

1 **Estimating ocean heat content from the ocean thermal expansion** 2 **parameters using satellite data**

3 Vijay Prakash Kondeti¹, Palanisamy Shanmugam¹

4 ¹Ocean Optics and Imaging Laboratory, Department of Ocean Engineering, Indian Institute of Technology Madras, Chennai-
5 600036, India

6 *Correspondence to:* Palanisamy Shanmugam (pshanmugam@iitm.ac.in)

7 **Abstract.** Ocean heat content (OHC) is a depth-integrated physical oceanographic variable used to precisely measure ocean
8 warming. Because of the limitations associated with in-situ CTD data and Ocean Reanalysis system products, satellite-based
9 approaches have gained importance in estimating the daily to decadal variability of OHC over the vast oceanic region. Efforts
10 to minimize the biases in satellite-based OHC estimates are needed to realize the actual response of the ocean to the brunt of
11 climate change. In the current study, an attempt has been made to better implement the satellite-based ocean thermal expansion
12 method to estimate OHC at 17 depth extents ranging from the surface to 700m. To achieve this objective, artificial neural
13 network (ANN) models were developed to derive thermosteric sea level (TSL) from a given dataset of sea surface temperature,
14 sea surface salinity, geographical coordinates, and climatological TSL. The model-derived TSL data were further used to
15 estimate OHC changes based on the thermal expansion efficiency of heat. Statistical analysis showed high correlation
16 coefficients and low errors in validation of satellite-derived TSL / OHC of 700 m modeling depth (N 388469, R 0.9926 /
17 0.9922, RMSE 1.16 m / 1.56 GJ m⁻², MBE -0.19 m / -0.24 GJ m⁻², MBPE -0.46% / -0.03%, MAE 0.76 m / 1.03 GJ m⁻², and
18 MAPE 2.34% / 0.13%) and nearly similar results at the remaining modeling depths. These results suggest that the proposed
19 ANN models are capable of generating satellite-based daily OHC maps by covering both shallower and deeper oceanic regions
20 of varying bathymetry levels (≥ 20 m). In addition, the first-ever attempt to estimate the ocean thermal expansion component
21 (*i.e.*, TSL) from satellite data was successful, and the model-derived TSL can be used to obtain high-end sea-level rise products
22 in the global ocean.

23 **1. Introduction**

24 Owing to the vast spatial coverage and high heat capacity, oceans balance the planet's temperatures by absorbing 89% of the
25 excess atmospheric heat caused by the greenhouse effect and global warming (Abraham et al., 2013; IPCC, 2014; Roemmich
26 et al., 2015; Riser et al., 2016; Trenberth et al., 2016; Meyssignac et al., 2019; Von Schuckmann et al., 2023). A precise
27 understanding of the depth-wise penetration of this heat and its accumulation in the upper oceanic layers is of great importance
28 to the scientific community (Liang et al., 2015; Baxter, 2016; IPCC, 2022). Ocean heat content (OHC), a depth-integrated
29 physical oceanographic variable that refers to the amount of heat energy accumulated between any two depths, has gained

30 attention in various studies of the Earth's Energy Imbalance (Von Schuckmann et al., 2016; Trenberth et al., 2016; Cheng et
31 al., 2017; Meyssignac et al., 2019; Cheng et al., 2022). Thus, accurate estimation of OHC changes at various depth extents is
32 vital and is the motivation of the current study.

33 To obtain a complete picture of OHC changes at different depths, direct measurements of in-situ conductivity,
34 temperature, and depth (CTD) profiles are necessary. These in-situ measurements of the ocean properties are limited in terms
35 of depth and spatial coverage, leading to the biased global reconstruction of OHC estimates owing to the sparse measurement
36 data and spatial coverage deficiencies (Jagadeesh et al., 2015; Meyssignac et al., 2019; Marti et al., 2022). However, in-situ
37 CTD profile measurements have been used to develop and validate the different OHC models (Momin et al., 2011; Jagadeesh
38 et al., 2015; Su et al., 2020; Vijay and Shanmugam, 2022). On the other hand, synthetic CTD profile data generated by Ocean
39 Reanalysis systems (ORA) have been used to study OHC variability in spatial and temporal scales (Balmaseda et al., 2015;
40 Palmer et al., 2017). More recently, satellite-based methods have become crucial to overcome the limitations associated with
41 in-situ CTD data and ORA products, to ensure the OHC trend at a global scale, and to understand the evolution of the Earth's
42 climate system (Meyssignac et al., 2019; Vijay and Shanmugam, 2022).

43 The existing satellite-based OHC algorithms can be broadly grouped into three approaches based on the
44 principles/parametrizations employed: (i) internal tide oceanic tomography (ITOT), (ii) ocean net surface heat fluxes, and (iii)
45 ocean thermal expansion. Apart from these approaches, research is exploring ways to make use of tidal magnetic satellite
46 observations (Irrgang et al., 2019), electrical conductance (Trossman and Tyler, 2019), and atmospheric oxygen & carbon
47 dioxide concentrations (Resplandy et al., 2018) to infer OHC changes. The ITOT technique involves correlating the satellite
48 altimeter-derived internal tide phase changes with ocean warming to estimate OHC variability. This technique is still at the
49 proof-of-concept level, and the associated challenges remain to be addressed (Zhao, 2016a, 2017; Meyssignac et al., 2019).
50 The OHC estimation through ocean net surface heat fluxes employs several assumptions and approximations in deriving the
51 input parameters to compute radiative and turbulent heat fluxes, which in turn leads to higher uncertainty in global OHC
52 changes (Wild et al., 2015; L'Ecuyer et al., 2015; Meyssignac et al., 2019).

53 On the other hand, the ocean thermal expansion method is a promising technique for the estimation of OHC by
54 considering the thermosteric sea level (TSL) and expansion efficiency of heat (EEH). Numerous satellite-based OHC models
55 have been developed based on the sea surface height anomaly from altimeters, water mass change equivalent sea level anomaly
56 from the Gravity Recovery and Climate Experiment mission (GRACE), sea surface temperature from the various radiometers
57 onboard satellites, and wind speed/stress from scatterometers/numerical weather models. Pioneering works done by White and
58 Tai (1995), Chambers et al. (1997), Polito et al. (2000), and Sato et al. (2000) have attempted to implement the ocean thermal
59 expansion method based on a relationship between OHC and satellite altimeter-based sea surface height anomaly (SSHA). It
60 should be mentioned that regardless of the source, the volume of seawater changes when it is subjected to heating/cooling, and
61 it eventually reflects in sea surface topography. The SSHA data recorded by the satellite altimeters comprise the sea surface
62 topography changes due to tides, atmospheric pressure, salinity (haline), and barotropic flows along with the thermal effects.
63 The SSHA changes due to the tides and atmospheric pressure can be corrected, but the effects of salinity and barotropic flows

64 remain unresolved with the OHC estimates produced by Wang and Tai (1995) and Chambers et al. (1997). Sato et al. (2000)
65 have introduced a haline correction factor as the integral product of the haline contraction coefficient and salinity anomaly
66 from in-situ CTD profile data. Owing to the limitations associated with in-situ data, the in-situ-based haline correction cannot
67 be applied to satellite altimeter-based SSHA data while correlating with the space and time-varying OHC data. Jayne et al.
68 (2003) have proposed the Alt-GRACE approach to resolve the effect of barotropic flows in sea surface topography by
69 subtracting the satellite gravimetry-derived water mass change component from SSHA data. Though the Alt-GRACE approach
70 has improved the accuracy of satellite-based OHC estimates compared to Wang and Tai (1995), Chambers et al. (1997), Polito
71 et al. (2000), and Sato et al. (2000), the issues associated with the haline effects and other approximations on the ocean thermal
72 expansion coefficient and seawater density data have led to significant uncertainties in satellite-based OHC estimates.

73 With the advancement of artificial intelligence, several researchers have attempted to model OHC by directly relating
74 it with the satellite-based parameters of relevance by using deep-learning regression techniques (Jagadeesh and Ali, 2006;
75 Momin et al., 2011; Chacko et al., 2015; Jagadeesh et al., 2015; Su et al., 2020, 2021; Marti et al., 2022; Lyman and Johnson,
76 2023). These deep-learning models have oversimplified the OHC problem by neglecting the effects of salinity and barotropic
77 flows. In addition, no previous work has accounted for the space and time-varying nature of the ocean thermal expansion
78 coefficient and seawater density in OHC computations. The other common drawbacks of the existing works are discussed in
79 Sect. 4.3. Consequently, there is a need for developing a satellite-based model to accurately implement the ocean thermal
80 expansion method to estimate OHC by resolving all the issues associated with salinity variation, barotropic flows, ocean
81 thermal expansion, seawater density, choice of temperature and its scale.

82 Given the above background, we have made a major attempt to develop and implement the satellite-based ocean
83 thermal expansion models for estimating OHC changes at various depth extents (such as 20 m, 30 m, 40 m, 50 m, 100 m, 150
84 m, 200 m, 250 m, 300 m, 350 m, 400 m, 450 m, 500 m, 550 m, 600 m, 650 m, and 700 m). It enables the research community
85 to generate satellite-based OHC maps of varying bathymetry levels (≥ 20 m) by covering both shallower and deeper oceanic
86 waters. For this, artificial neural network (ANN) architectures were developed to estimate TSL for the given sea surface
87 temperature (SST), sea surface salinity (SSS), geographical coordinates, and climatological TSL. The model-derived TSL
88 estimates were then used to model OHC changes by accounting for the expansion efficiency of heat. The proposed models are
89 capable of estimating TSL and OHC at multiple depth extents accurately. The robustness of the new models was tested by
90 comparison of model-derived TSL and OHC with in-situ data.

91 **2. Data**

92 **2.1. In-situ data for model development and in-situ validation**

93 For this study, in-situ CTD profile data (collected by Argo floats) were obtained from the World Ocean Database-2018 (WOD)
94 at the NOAA's National Centers for Environmental Information data archive for the period of 2005-2020 (Boyer et al., 2018a).
95 WOD has been extensively used by the research community for various ocean applications (Levitus et al., 2009; Momin et al.,

96 2011; Levitus et al., 2012; Cheng et al., 2014; Roemmich et al., 2015; Jagadeesh et al., 2015; Su et al., 2020). WOD comprises
 97 the oceanographic data of diverse biogeochemical parameters that have been collected by various institutions, agencies,
 98 individual researchers, and data recovery initiatives. The quality-controlled CTD profile data (*accepted_value* flag) of standard
 99 depth levels recommended by the International Association of Physical Oceanography (1936) were considered in this study to
 100 compute the TSL_d and OHC_d parameters and to obtain the SST and SSS data. The standard depth levels considered for deriving
 101 the TSL and OHC are given as 20 m, 30 m, 40 m, 50 m, 100 m, 150 m, 200 m, 250 m, 300 m, 350 m, 400 m, 450 m, 500 m,
 102 550 m, 600 m, 650 m, and 700 m. The in-situ TSL_d and OHC_d parameters were computed by applying the integration formulae
 103 (Eqs. 1 & 2) on the CTD profile data of depth range from the ocean surface to the respective standard depth (d), and the
 104 corresponding SST and SSS values were extracted. Similarly, the climatological parameters such as $TSL_{clim,d}$ and $OHC_{clim,d}$
 105 were computed from the monthly climatological temperature and salinity data of 41 vertical levels obtained from the World
 106 Ocean Atlas-2018 (WOA) (Boyer et al., 2018b). The theoretical considerations for computing OHC change at a particular
 107 depth can be found in Vijay and Shanmugam (2022) (Vijay and Shanmugam, 2022), and the same was adopted in this study.
 108 The Gibbs-SeaWater (GSW) Oceanographic Toolbox of TEOS-10 (IOC et al., 2010) was used to compute the in-situ-based
 109 OHC and TSL.

$$110 \quad OHC_d = \int_0^d \rho C_P \theta dz \quad (1)$$

$$111 \quad TSL_d = \int_0^d \alpha \theta dz \quad (2)$$

112 where OHC_d refers to the heat energy accumulated in an oceanic layer of depth range from the surface to a stipulated depth
 113 (d) and is given in the units of joules per unit area ($J m^{-2}$). Similarly, TSL_d (in meters) refers to the thermosteric sea level
 114 integrated from the surface to a stipulated depth (d). And, θ is the conservative temperature in K (derived from in-situ
 115 temperature, absolute salinity, and pressure), ρ is the seawater density in $kg m^{-3}$ (derived from the conservative temperature,
 116 absolute salinity, and pressure), C_P is the specific heat capacity ($= 3991.87 J kg^{-1} K^{-1}$), and α is the thermal expansion coefficient
 117 in K^{-1} (derived from the conservative temperature, absolute salinity, and pressure).

118 Python programming was used to prepare the individual databases for all the standard depth levels by extracting CTD
 119 profile data from the WOD and WOA NetCDF files with the help of NetCDF4, NumPy, Pandas, and GSW libraries. Each
 120 database (in-situ OHC, in-situ TSL, in-situ SST, in-situ SSS, climatological OHC, climatological TSL, and WOA geographical
 121 coordinates) was divided into two datasets, one for the model development spanning from 2005-2016 and the other for
 122 validating the model spanning from 2017-2020, by ensuring a well distribution in spatiotemporal scales over the global open
 123 ocean. The spatial distribution of data points used to model TSL_{700} and OHC_{700} is shown in Fig. A1. The in-situ CTD profiles
 124 of depth coverage shallower than 700 m are also included in this process of deriving the TSL and OHC of remaining depth
 125 extents. Indeed, the number of CTD profiles and their distribution in global oceans is higher than the CTD profile density of
 126 modeling depth 700 m.

127 2.2. Satellite-based validation

128 For the validation period 2017-2020, the NOAA Advanced Very High-Resolution Radiometer (AVHRR) Optimum
129 Interpolation Sea Surface Temperature product (OISST v2.1) was used for daily SST data at 0.25° spatial resolution (Huang
130 et al., 2021). Daily SSS data of the same spatial resolution were obtained from the ORAS5 Ocean reanalysis system of the
131 European Centre for Medium-Range Weather Forecasts at the CMEMS portal (Product ID:
132 GLOBAL_REANALYSIS_PHY_001_031) (Zuo et al., 2017). The NetCDF4 and NumPy Python libraries were used to read
133 and resample satellite data to the WOA-18 grid and to collocate with the corresponding Argo in-situ data points. The accuracy
134 of the satellite-based SST and ORA-based SSS was verified by comparing with Argo-measured SST and SSS data (N =
135 244722). The observed R, RMSE, MBE, and MAE values in SST & SSS validations are 0.99 & 0.99, 0.51°C & 0.26 PSU, -
136 0.05°C & -0.006 PSU, and 0.33°C & 0.12 PSU, respectively. High correlation coefficients and low errors indicate the minimal
137 deviation of satellite-based data from the actual (in-situ) data and ensure the reliability of satellite data in accurately
138 representing the physical oceanographic conditions.

139 3. Methodology

140 3.1. Theoretical formulations

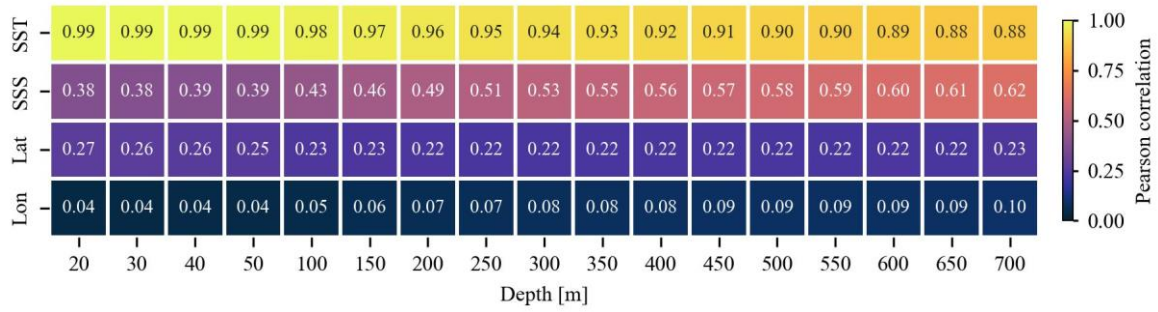
141 Ocean thermal expansion is the best proxy to model the heat content accumulated in an oceanic layer. Unlike freshwater,
142 seawater expands when it warms and contracts when it cools to temperatures above its freezing point. The volumetric
143 expansion of seawater is non-isotropic in nature due to the differences in the degree of constraint in different directions. In a
144 vertical direction, atmospheric pressure exerts a normal force on the seawater parcel at the surface. The magnitude of this
145 normal/vertical force is less compared to the horizontal forces exerted by physical barriers such as continental boundaries and
146 geographic features on the ocean floor. It allows the ocean thermal expansion of seawater in the vertical direction rather than
147 the horizontal direction, as the seawater is less constrained in the vertical direction compared to the horizontal direction. The
148 amount of change in seawater volume in response to the net warming/cooling depends on the absolute conservative temperature
149 and ocean thermal expansion coefficient (Eq. 2). Following are the GSW functions (Eqs. 3-5) (IOC et al., 2010) involved in
150 the calculation of TSL (Eq. 2) for the given set of measured temperature (T), practical salinity (SP), pressure (P), longitude
151 (x), and latitude (y).

$$152 \text{ Absolute salinity } (SA) = gsw.SA_from_SP(SP, P, x, y) \quad (3)$$

$$153 \theta = gsw.CT_from_T(SA, T, P) \quad (4)$$

$$154 \alpha = gsw.Alpha(SA, \theta, P) \quad (5)$$

155 Hence, an attempt has been made in this study to model TSL as a function of SST, SSS, and geographical coordinates. The
156 existing correlations between the proposed input parameters and the targeted output parameter were explored by employing
157 in-situ-based data used in the model development process (Fig. 1).



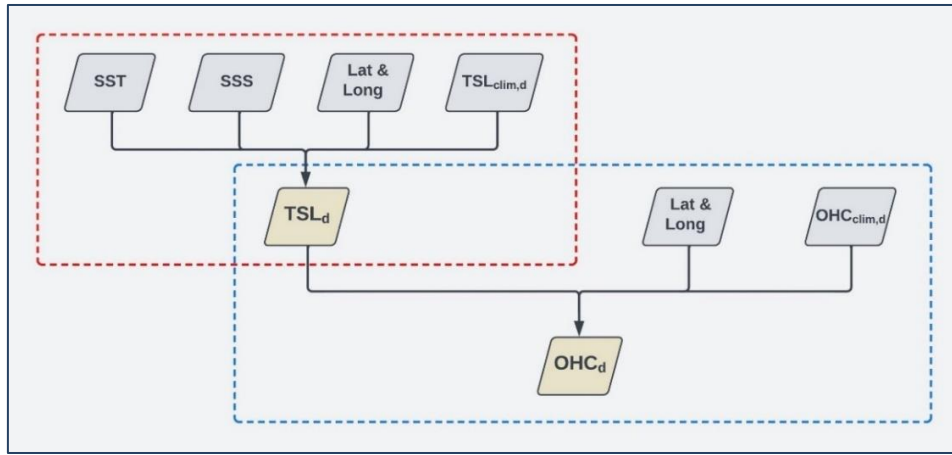
158

159 **Figure 1.** Heatmap showing the Pearson correlation coefficients between the input parameters (*i.e.*, SST, SSS, and
 160 geographical coordinates) and the output parameter (TSL) of various depth extents.

161 It is observed that SST has an almost one-to-one correlation with TSL at shallower depth extents, and can be solely
 162 used to model the thermal expansion of upper oceanic layers. Despite a decreasing trend in correlation strength when moving
 163 towards deeper depths, SST plays a primary role in accounting for TSL variations at deeper depths, because of its strong
 164 correlations with TSL. Observed weaker correlations between SSS and TSL which are plausible owing to the salinity's
 165 secondary role in TSL variations as compared to the temperature. However, an increasing trend in correlation coefficients
 166 between SSS and TSL is observed towards the deeper depth extents. Hence, SST and SSS are complementary to each other in
 167 resolving the TSL variations, and their combination plays a major role in modeling TSL of all depth extents considered in this
 168 study. Apart from these physical parameters, absolute salinity used in the computation of seawater density, conservative
 169 temperature, and ocean thermal expansion coefficient is a function of geographical coordinates along with practical salinity
 170 and pressure (Eq. 3). By considering all these theoretical considerations and observed correlations, an attempt has been made
 171 to model TSL of various depth extents by employing SST, SSS, and geographical coordinates as the input parameters along
 172 with the climatological TSL (Fig. 2). Here, TSL_d is an external manifestation of OHC_d stored in an oceanic layer based on
 173 EEH_d (Eq. 6). The model-derived TSL is further used to estimate OHC changes (as shown in Fig. 2 along with climatological
 174 OHC) as follows,

$$175 \quad OHC_d = \frac{TSL_d}{EEH_d} \quad (6)$$

176 where EEH is a conversion factor that explains the relationship between the relative changes in OHC and the corresponding
 177 TSL. EEH is not a constant value over the global ocean as it varies as a function of temperature, salinity, and pressure. Hence,
 178 ANN modeling is employed in this study to estimate OHC from TSL by accounting the complex variations in EEH .



179

180 **Figure 2.** Flow chart representing the parameters involved in TSL and OHC modeling. The red and blue dashed boxes represent
 181 the TSL and OHC frameworks employed in ANNs, respectively.

182

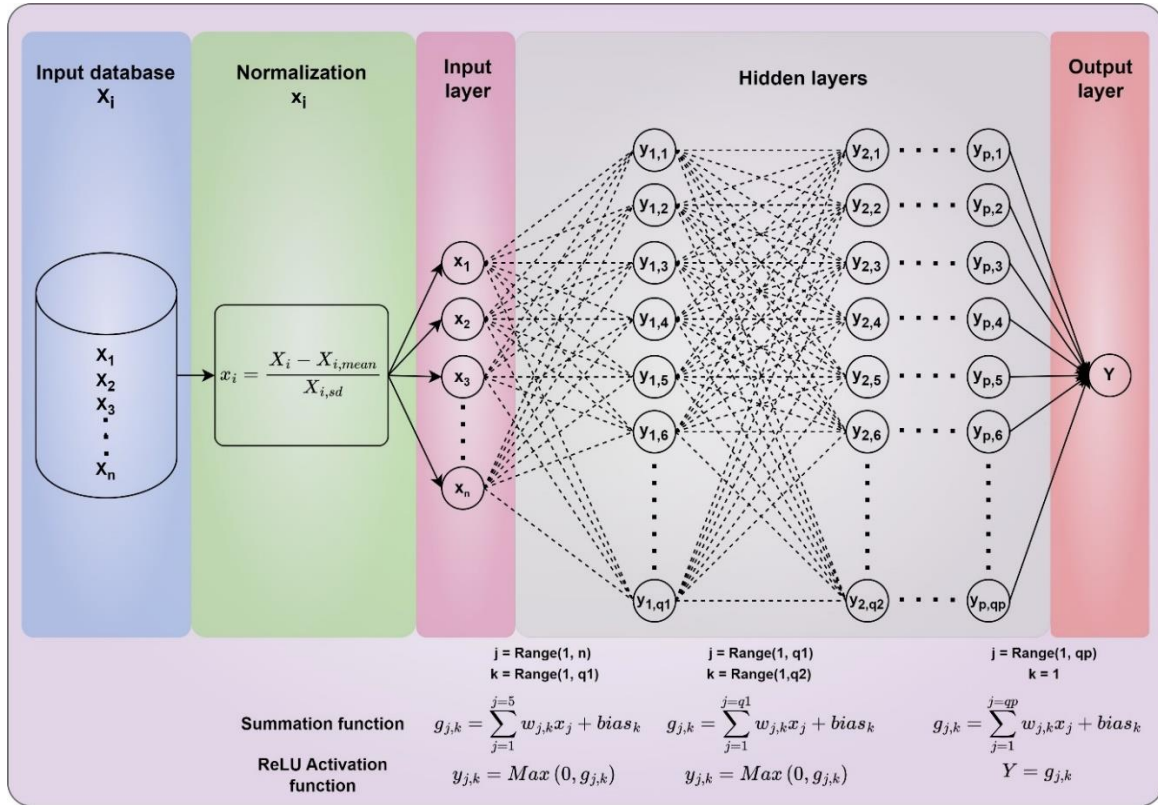
183 3.2. ANN model description

184 This section explains the various steps and architectures involved in the ANN modeling of TSL and OHC. The multilayer
 185 perceptron regressor algorithm of deep neural networks was used to model both TSL and OHC (Pedregosa et al., 2011). It is
 186 observed that the input data of geophysical parameters have different units and scales. The range and order of SST, SSS,
 187 latitude, and longitude data are $-1.8\text{ }^{\circ}\text{C}$ to $34.15\text{ }^{\circ}\text{C}$ & $O(10^1)$, 2.53 PSU to 40.45 PSU & $O(10^1)$, -76° to 80° & $O(10^1)$, and $-$
 188 180° to 180° & $O(10^2)$, respectively. In addition, the range and order of $\text{TSL}_{\text{clim,d}}$ and $\text{OHC}_{\text{clim,d}}$ are also distinct and vary with
 189 water depth. Hence, the input data were normalized using the StandardScaler class of Scikit-Learn and feed-forwarded through
 190 the neural networks. This StandardScaler normalizes the raw data to ensure the mean and standard deviation of each input
 191 parameter as 0 and 1, respectively. It allows the ANN model to focus on the relative importance and relationships between the
 192 input parameters rather than their magnitude. The standardized input data were injected into the corresponding neurons in the
 193 input layer and forward propagated through the hidden layers and then the output layer by applying the random weights and
 194 rectified linear unit (ReLU) activation function at each neuron (Fig. 3). The model outputs were compared with the actual data
 195 and computed mean squared error (MSE) using a loss function (Eq. 7). In addition, L2 regularization (α_{L2}) was employed to
 196 add a penalty term to the loss value to prevent overfitting. The observed error was then backpropagated through the network
 197 to update weights and biases using the Adam optimizer based on the learning rate and gradient of the error (see Eq. 8 in Vijay
 198 and Shanmugam, 2022). This process is repeated until the validation score improves more than 0.0001.

$$199 \text{MSE} = \frac{1}{N} \sum (Y_{\text{pred},i} - Y_{\text{act},i})^2 \quad (7)$$

200 where N is the number of samples, $Y_{\text{pred},i}$ is the predicted data, and $Y_{\text{act},i}$ is the actual data. The model development work was
 201 carried out by employing both the input and output parameters from the in-situ sources. It enables the ANN models to
 202 implement the input data of any remote sensing sources to produce OHC estimates subject to the reliability and accuracy of

203 those data sources. The particle swarm optimization technique (Kennedy and Eberhart, 1995; Shi and Eberhart, 1998) was
 204 employed for hyperparameter tuning, and the hyperparameters' combinations corresponding to each modeling depth are
 205 presented in Table 1. The Joblib module of the Scikit-Learn library was used to save all the TSL and OHC models of various
 206 depths considered in this study, and the same module was used to load the TSL and OHC models of desired depth with the
 207 help of a unified Python script.



208
 209 **Figure 3.** Schematic of the ANN architecture employed in the modeling of TSL and OHC parameters. The flow of the
 210 modeling and the associated mathematical transformations/formulations are given by considering a typical ANN architecture
 211 with n input parameters, one output parameter, p hidden layers, and $q1$ to qp neurons in each hidden layer.

212
 213
 214
 215
 216
 217
 218
 219

220 **Table 1.** ANN model hyperparameters employed in TSL (regular font) and OHC (bold font) modeling of various depth extents.

Depth (m)	Hidden layers	Batch size	α_{L2}	Learning rate	No. of iterations
20	38, 10, 55	178	0.00422	0.0004	14
	49, 12, 34	183	0.09023	0.0001	26
30	100, 97, 36	165	0.00001	0.0001	14
	11, 50, 55	58	0.00079	0.0001	16
40	64, 71, 5	106	0.00001	0.0001	16
	57, 89, 46	148	0.09691	0.0001	19
50	64, 99, 30	241	0.01478	0.0001	17
	56, 59, 10	139	0.07188	0.0001	22
100	70, 100, 100	256	0.00001	0.0009	30
	25, 36, 63	256	0.03556	0.0016	44
150	47, 83, 92	60	0.00001	0.0005	34
	49, 77, 28	69	0.05176	0.0318	16
200	100, 100, 16	256	0.00315	0.0022	33
	27, 48, 67	202	0.05638	0.0367	18
250	56, 82, 67	174	0.00001	0.0019	39
	2, 100, 77	73	0.00001	0.0037	22
300	83, 28, 74	128	0.00001	0.0028	36
	48, 92, 10	87	0.01364	0.0459	12
350	85, 25, 67	128	0.04606	0.0013	20
	27, 53, 48	141	0.08585	0.0851	14
400	89, 75, 96	64	0.04859	0.0007	26
	49, 1, 80	138	0.00001	0.0031	20
450	51, 83, 95	128	0.08582	0.0005	42
	47, 27, 52	32	0.00263	0.0055	24
500	71, 100, 62	128	0.00001	0.0012	27
	45, 100, 63	126	0.05162	0.0607	15
550	47, 89, 91	256	0.00843	0.0011	44
	64, 75, 78	114	0.05176	0.0634	15
600	98, 65, 6	16	0.00001	0.0001	48
	63, 17, 10	180	0.04654	0.0538	23
650	100, 69, 75	16	0.00001	0.0001	18
	53, 74, 40	176	0.07072	0.0048	20
700	98, 37, 37	164	0.04262	0.0015	32
	83, 63, 79	216	0.01217	0.0742	19

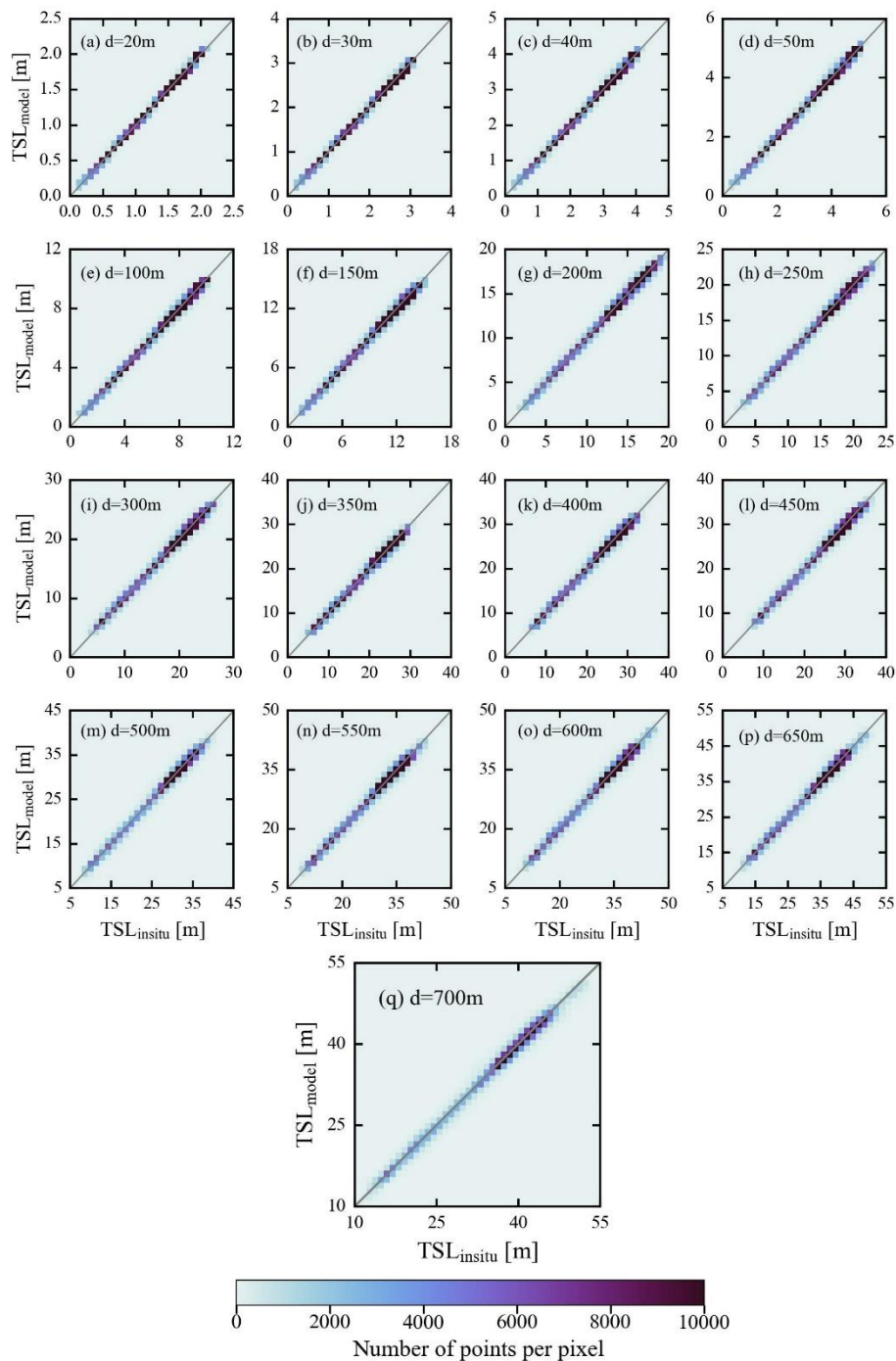
221 **4. Results and discussion**

222 The performance of TSL and OHC models on unseen data from the in-situ and satellite sources was assessed using density
223 scattergrams and statistical metrics. These metrics include mean bias error (MBE), mean bias percentage error (MBPE), mean
224 absolute error (MAE), mean absolute percentage error (MAPE), root mean square error (RMSE), Pearson correlation
225 coefficient (R), slope, and intercept (also referred and presented in Vijay and Shanmugam, 2022). To better understand the
226 model performance, mean values of in-situ data were computed for the validation period and used to compute the weighted
227 average of validation metrics across all the modeling depths.

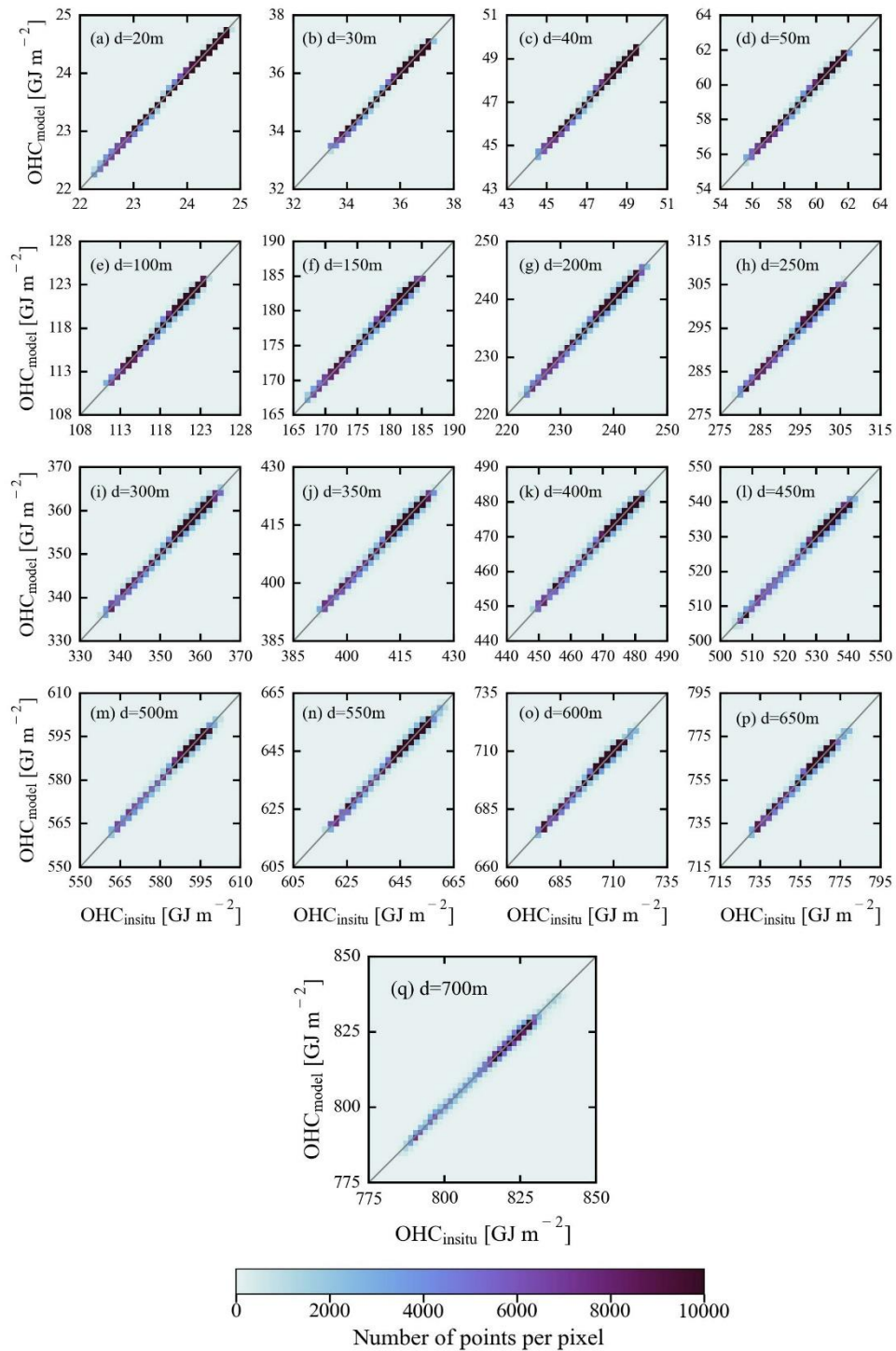
228 **4.1 In-situ validations with unseen data**

229 The main objective of the in-situ-based validation with unseen data is to evaluate the generalization ability and overall accuracy
230 of TSL and OHC-ANN models on unseen data. For this purpose, the in-situ measured data of SST, SSS, latitude, and longitude
231 were used to predict the model-derived TSL and OHC values, which were then compared with in-situ TSL and OHC data. The
232 number of validation data points and their spatial distribution are presented in Table 2 and Fig. A1(b). The performance of the
233 TSL models is exceptionally good on unseen data of all the modeling depths without any overfitting (Table 2 and Fig. 4).
234 Similar model performance can also be observed in the case of OHC estimates as it primarily depends on the TSL estimates
235 (Table 2 and Fig. 5). The high values of R indicate a strong positive correlation between the predicted and in-situ OHC (TSL)
236 values. This suggests that the models are generally capable of capturing OHC (TSL) patterns in the data. The slope and
237 intercept of the regression line between predicted and actual values are close to 1 and 0, respectively. This suggests that the
238 model-derived estimates have good agreement with the actual data with a minimal bias. The RMSE values are notably small
239 implying that the predicted OHC values have a little random error when compared to the actual data. The MBE and MBPE
240 values are close to zero, indicating that the model-derived estimates have a negligible systematic error when compared to the
241 actual values. The low MAE and MAPE values are also indicating a high accuracy with the model-predicted OHC values.
242 These results clearly demonstrate that the proposed ANN models succeeded in generalizing and accurately predicting the OHC
243 (TSL) data with a high accuracy.

244 The spatial distribution of mean percentage error (MPE) over the global open oceanic regions was computed by
245 averaging the observed percentage errors of all modeling depths available at each pixel (Fig. A2). It is observed that the models'
246 performance is comparatively low over the north-western parts of the North Atlantic gyre, southwestern parts of the South
247 Atlantic gyre, Kuroshio extension, and Antarctic circumpolar current regions due to the high eddy kinetic energy (Beech et
248 al., 2022; Ni et al., 2023). An elaborate note on the potential sources of the observed MPE values is given in Sect. 4.4. Further,
249 the entire validation dataset was divided into two parts in terms of the observed overestimation and underestimation of data.
250 In the cases of overestimation (underestimation), 95% of the data points have MPE of less than or equal to 0.47% (0.44%).
251 The lower values of MPE indicate that the proposed ANN models are capable of capturing OHC patterns in all major oceanic
252 basins and can be used to produce accurate OHC products upon implementation on real-time data.



253
 254 **Figure 4.** Density scattergrams showing the observed agreement between model-derived TSL values and in-situ measured
 255 TSL values during in-situ-based validations.



256
 257 **Figure 5.** Density scatterplots showing the observed agreement between model-derived OHC values and in-situ measured
 258 OHC values during in-situ-based validations.

259 **Table 2.** Statistical results from the in-situ-based validation of TSL (regular font) and OHC (bold font) against in-situ data.
 260 The units for the various metrics used in TSL & OHC validations are given as follows: Mean (m & GJ m⁻²), RMSE (m & GJ
 261 m⁻²), MBE (m & GJ m⁻²), MBPE (%), MAE (m & GJ m⁻²), MAPE (%), and intercept (m & GJ m⁻²).

Depth (m)	N		Mean	R	RMSE	MBE	MBPE	MAE	MAPE	Slope	Intercept
	Model development	Model validation									
20	801303	536719	1.44	0.9997	0.01	-0.0007	0.0575	0.006	0.60	0.9981	0.002
			23.91	0.9997	0.02	-0.0011	-0.0047	0.009	0.04	0.9987	0.030
30	794166	532149	2.15	0.9993	0.03	0.0029	0.3764	0.015	0.99	0.9982	0.007
			32.85	0.9992	0.04	0.0010	0.0027	0.021	0.06	0.9992	0.030
40	787074	526571	2.85	0.9988	0.05	-0.0009	0.1325	0.027	1.28	0.9988	0.002
			47.78	0.9988	0.07	-0.0008	-0.0014	0.038	0.08	0.9978	0.103
50	779134	520102	3.54	0.9984	0.07	-0.0008	0.0861	0.042	1.47	0.9975	0.008
			59.70	0.9984	0.10	0.0015	0.0028	0.057	0.10	0.9972	0.169
100	731065	476709	6.80	0.9974	0.18	-0.0129	-0.1725	0.120	2.09	0.9960	0.015
			119.00	0.9973	0.25	-0.0279	-0.0233	0.169	0.14	0.9981	0.196
150	712120	460278	9.83	0.9967	0.29	-0.0407	-0.3419	0.205	2.41	0.9905	0.053
			177.97	0.9965	0.40	-0.0369	-0.0198	0.279	0.16	0.9867	2.331
200	697314	446979	12.64	0.9961	0.38	-0.0001	0.0571	0.272	2.51	0.9960	0.050
			236.62	0.9959	0.53	-0.0076	-0.0029	0.372	0.16	0.9939	1.426
250	686378	436906	15.28	0.9959	0.46	-0.0361	-0.1803	0.332	2.49	0.9943	0.051
			295.04	0.9957	0.63	-0.0242	-0.0078	0.450	0.15	0.9918	2.392
300	678526	429501	17.80	0.9956	0.55	-0.0471	-0.0023	0.392	2.53	0.9851	0.218
			353.29	0.9954	0.74	-0.0155	-0.0039	0.525	0.15	0.9889	3.902
350	672148	423688	20.23	0.9949	0.65	-0.1035	-0.3383	0.462	2.59	0.9860	0.179
			411.40	0.9947	0.87	-0.0357	-0.0081	0.613	0.15	0.9861	5.676
400	666605	418686	22.57	0.9947	0.72	-0.0425	-0.0526	0.505	2.52	0.9887	0.213
			469.39	0.9945	0.97	-0.0067	-0.0010	0.676	0.14	0.9879	5.683
450	661336	413987	24.83	0.9946	0.78	-0.1227	-0.4726	0.547	2.47	0.9916	0.087
			527.25	0.9943	1.06	-0.1681	-0.0315	0.741	0.14	0.9872	6.588
500	654880	408240	27.03	0.9949	0.80	-0.0604	-0.1866	0.558	2.29	0.9945	0.089
			585.03	0.9947	1.07	-0.0761	-0.0127	0.747	0.13	0.9894	6.105
550	649850	403357	29.14	0.9948	0.85	-0.0462	-0.0937	0.586	2.19	0.9911	0.213
			642.69	0.9945	1.15	0.0347	0.0057	0.787	0.12	0.9900	6.479
600	645150	398855	31.21	0.9945	0.91	-0.0390	-0.0205	0.623	2.18	0.9883	0.327
			700.28	0.9942	1.23	0.0298	0.0046	0.838	0.12	0.9873	8.937
650	640479	392921	33.18	0.9941	0.99	0.0185	0.0903	0.670	2.19	0.9949	0.189
			757.74	0.9939	1.33	0.0086	0.0014	0.892	0.12	0.9904	7.296
700	633004	388469	35.13	0.9941	1.04	-0.1928	-0.4791	0.711	2.17	0.9858	0.307
			815.15	0.9938	1.41	-0.2413	-0.0292	0.960	0.12	0.9836	13.134
Weighted average				0.9961	0.74	-0.0620	-0.1591	0.513	2.29	0.9927	0.177
				0.9960	1.03	-0.0515	-0.0087	0.708	0.13	0.9914	6.648

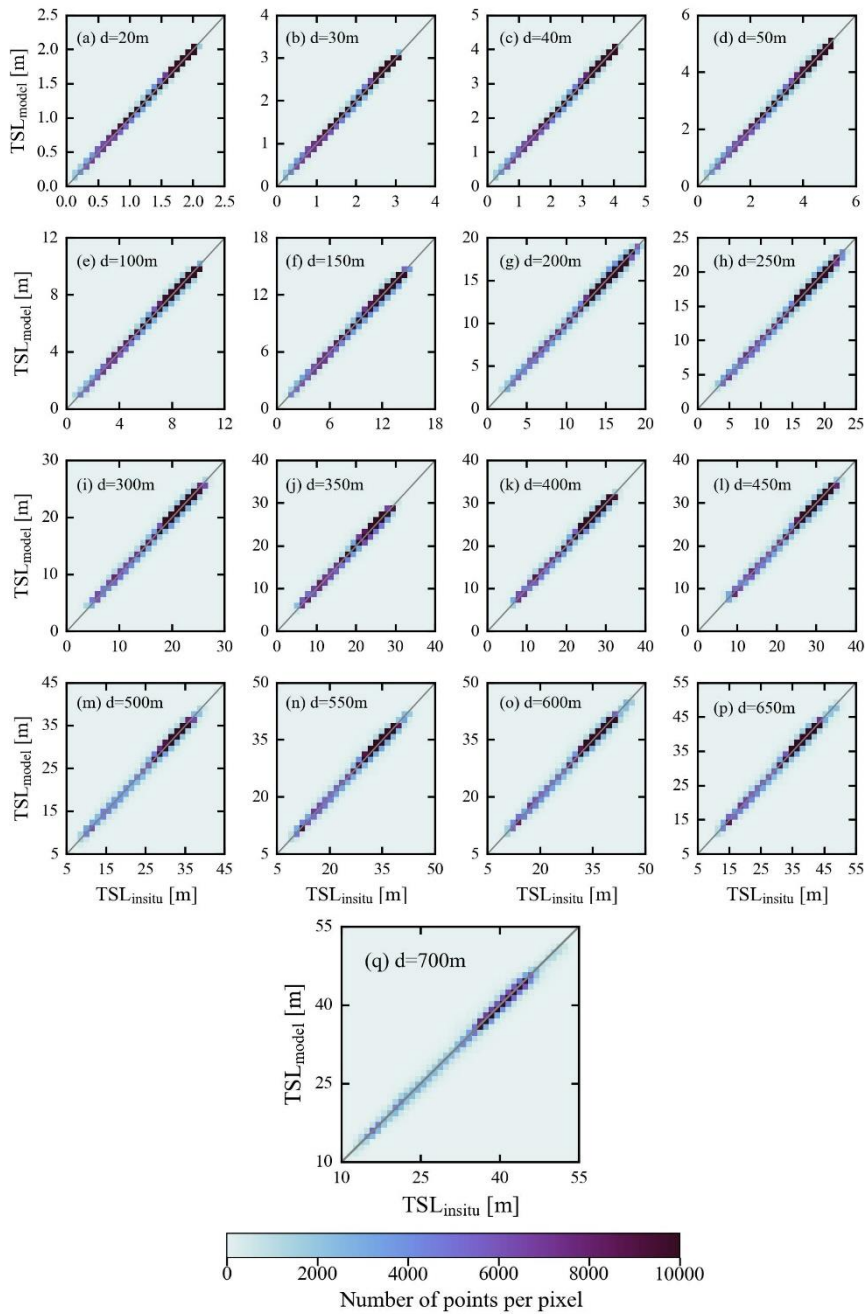
262

263 4.2. Satellite-based validations with unseen data

264 The performance of the proposed ANN models in satellite-based applications has been assessed by injecting daily SST and
 265 SSS data from the satellite sources (refer to Sect. 2.2) in place of in-situ sources. The choice of satellite sources for SST and

266 SSS data is completely subjective to the intended application and their compatibility in terms of spatial and temporal
267 resolutions, whereas geographical coordinates data can be employed from WOA corresponding to the climatological TSL and
268 OHC data. It is recommended to resample SST and SSS data to the WOA grid to eliminate the discrepancies arising from the
269 non-uniform spatial references among the input data. The satellite-based SST, ORA-based SSS, latitude, and longitude data
270 were then given as the inputs to the ANN models for producing TSL and OHC estimates of all the modelling depths considered
271 in this study. Consequently, the model-derived TSL and OHC estimates were compared with Argo-measured in-situ data, and
272 the observed validation results are presented in this section (Table 3 and Figs. 6 and 7).

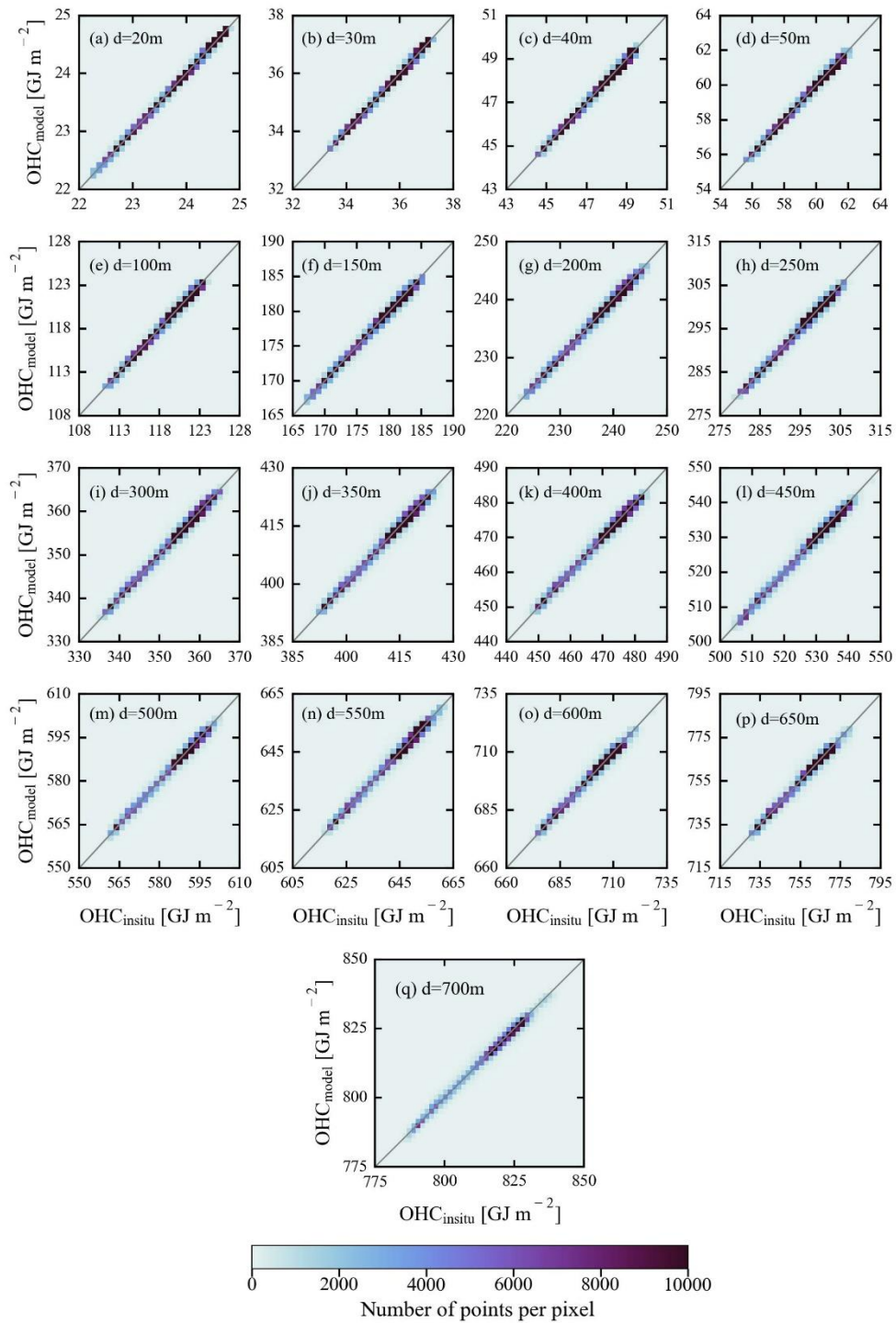
273 The performance of the proposed ANN models on satellite-based validation data (Table 3, Figs. 6 and 7) is almost
274 similar to their performance on in-situ-based validation data (Table 2, Figs. 4 and 5). However, the models' performance on
275 satellite-based validation data was marginally low as compared to the in-situ-based validation, likely due to the errors
276 associated with the satellite-based products. According to the statistical results, the R values were observed to be slightly lower
277 by an average percentage decrease of 0.11% across all the modeling depths. Similarly, the RMSE, MBE, MBPE, MAE, and
278 MAPE values were slightly larger than those observed during the in-situ-based validation. This relatively lower performance
279 of the proposed models on the satellite-based validation datasets can be observed by comparing the spatial maps and the
280 distribution of MPE (Figs. A2 and A3). And, 95% of the data have MPE of less than or equal to 0.56% (0.5%) in the cases of
281 overestimation (underestimation), which is higher than those reported in Sect. 4.1. Though the performance of the proposed
282 models on satellite-based data is comparatively lower than the in-situ-based validation, the observed difference in various
283 validation metrics is insignificant. It indicates the efficiency of the proposed models in estimating OHC from satellite data at
284 various depths over the major oceanic basins. However, it should be noted that the validation results presented in this section
285 are subject to vary with the other sources of satellite-based SST and SSS data.



286

287 **Figure 6.** Density scatterplots showing the observed agreement between model-predicted TSL values and in-situ measured

288 TSL values during satellite-based validation.



289

290 **Figure 7.** Density scatterplots showing the observed agreement between model-predicted OHC values and in-situ measured

291 OHC values during satellite-based validation.

292 **Table 3.** Statistical results from satellite-based validation data of TSL (regular font) and OHC (bold font) against unseen Argo
 293 measured in-situ data. The units for the various metrics used in TSL & OHC validations are given as follows: Mean (m & GJ
 294 m⁻²), RMSE (m & GJ m⁻²), MBE (m & GJ m⁻²), MBPE (%), MAE (m & GJ m⁻²), MAPE (%), and intercept (m & GJ m⁻²).

Depth (m)	N		Mean	R	RMSE	MBE	MBPE	MAE	MAPE	Slope	Intercept
	Data for model development	Data for model validation									
20	801303	536719	1.44	0.9987	0.03	-0.0034	-0.0822	0.016	1.67	0.9960	0.002
			23.91	0.9987	0.04	-0.0049	-0.0201	0.023	0.09	0.9965	0.080
30	794166	532149	2.15	0.9984	0.04	-0.0008	0.2562	0.027	1.88	0.9961	0.008
			32.85	0.9984	0.06	-0.0043	-0.0118	0.037	0.10	0.9969	0.108
40	787074	526571	2.85	0.9980	0.07	-0.0054	0.0211	0.041	2.08	0.9969	0.003
			47.78	0.9980	0.09	-0.0070	-0.0143	0.057	0.12	0.9959	0.191
50	779134	520102	3.54	0.9977	0.09	-0.0060	-0.0262	0.057	2.17	0.9960	0.008
			59.70	0.9976	0.12	-0.0056	-0.0090	0.077	0.13	0.9956	0.257
100	731065	476709	6.80	0.9966	0.20	-0.0206	-0.2651	0.140	2.56	0.9951	0.013
			119.00	0.9965	0.28	-0.0385	-0.0322	0.194	0.16	0.9971	0.301
150	712120	460278	9.83	0.9958	0.32	-0.0496	-0.4165	0.229	2.81	0.9897	0.052
			177.97	0.9956	0.44	-0.0491	-0.0266	0.311	0.17	0.9858	2.474
200	697314	446979	12.64	0.9951	0.43	-0.0091	-0.0022	0.300	2.83	0.9951	0.053
			236.62	0.9950	0.59	-0.0200	-0.0081	0.409	0.17	0.9929	1.653
250	686378	436906	15.28	0.9948	0.52	-0.0450	-0.2117	0.364	2.79	0.9928	0.065
			295.04	0.9946	0.71	-0.0365	-0.0119	0.492	0.17	0.9904	2.807
300	678526	429501	17.80	0.9943	0.62	-0.0556	-0.0279	0.428	2.79	0.9837	0.235
			353.29	0.9941	0.83	-0.0271	-0.0071	0.571	0.16	0.9875	4.398
350	672148	423688	20.23	0.9939	0.71	-0.1052	-0.3291	0.494	2.80	0.9846	0.206
			411.40	0.9936	0.95	-0.0381	-0.0086	0.655	0.16	0.9847	6.264
400	666605	418686	22.57	0.9935	0.79	-0.0450	-0.0422	0.540	2.72	0.9869	0.252
			469.39	0.9933	1.06	-0.0103	-0.0017	0.723	0.15	0.9860	6.557
450	661336	413987	24.83	0.9934	0.87	-0.1234	-0.4559	0.586	2.67	0.9898	0.129
			527.25	0.9931	1.17	-0.1694	-0.0316	0.792	0.15	0.9854	7.508
500	654880	408240	27.03	0.9934	0.91	-0.0707	-0.2034	0.605	2.50	0.9924	0.134
			585.03	0.9933	1.21	-0.0909	-0.0151	0.807	0.14	0.9874	7.293
550	649850	403357	29.14	0.9932	0.97	-0.0484	-0.0768	0.636	2.40	0.9887	0.280
			642.69	0.9929	1.30	0.0315	0.0053	0.851	0.13	0.9876	8.021
600	645150	398855	31.21	0.9930	1.03	-0.0431	-0.0139	0.675	2.38	0.9861	0.392
			700.28	0.9927	1.39	0.0242	0.0039	0.906	0.13	0.9850	10.52
650	640479	392921	33.18	0.9926	1.11	0.0193	0.1132	0.719	2.37	0.9925	0.267
			757.74	0.9924	1.48	0.0092	0.0015	0.957	0.13	0.9880	9.090
700	633004	388469	35.13	0.9926	1.16	-0.1917	-0.4560	0.763	2.34	0.9835	0.387
			815.15	0.9922	1.56	-0.2400	-0.0290	1.029	0.13	0.9813	14.982
Weighted average			0.9950	0.83	-0.0657	-0.1645	0.554	2.54	0.9909	0.224	
			0.9948	1.15	-0.0566	-0.0104	0.763	0.14	0.9896	7.799	

295

296 **4.3. Comparison with the contemporary satellite-based OHC models**

297 Comparison of our ANN models with the existing models is crucial to determine the relative uncertainty in the OHC estimates.
 298 Previously, an ANN algorithm suite was developed by the National Remote Sensing Centre (NRSC) of ISRO to disseminate
 299 the daily OHC products over the North Indian Ocean (40°E-120°E, 0°-30°N) at a spatial resolution of 0.25 degree (Ali et al.,
 300 2012; Jagadeesh et al., 2015). This algorithm suite includes ANN models to estimate OHC at multiple depth extents such as
 301 50 m, 100 m, 150 m, 200 m, 300 m, 500 m, and 700 m for the given input data of SSHA, SST, and $OHC_{clim,d}$. NRSC-ANN
 302 models estimate OHC changes by employing the satellite altimetry-based SSHA data from AVISO (Archiving, Validation,
 303 and Interpretation of Satellite Oceanographic data) data portal, SST from the Advanced Microwave Scanning Radiometer-2
 304 onboard JAXA's Global Change Observation Mission - Water (GCOM-W1), and climatological OHC from the World Ocean
 305 Atlas-2009 monthly climatological CTD profiles. The multilayer perceptron regressor algorithm of neural networks with three
 306 hidden layers was used to estimate OHC of all seven depth extents. The number of data points used to develop and validate
 307 the NRSC-ANN algorithm were 11472 and 2479, respectively. To compute in-situ OHC at different depths, this algorithm
 308 employed the Celsius scale, in-situ temperature, and average density data instead of the Kelvin scale, conservative temperature,
 309 and instantaneous density, respectively (see Eq. 3 in Jagadeesh et al., 2015).

310 Validation datasets were prepared for the period of 2017-2020 by computing in-situ OHC in both Kelvin and Celsius
 311 scales for the depth extents of 50 m, 100 m, 150 m, 200 m, 300 m, 500 m, and 700 m from Argo program. Daily OHC data
 312 were downloaded from the NRSC's Bhuvan portal and collocated with the corresponding Celsius-scaled in-situ OHC data to
 313 evaluate the NRSC-ANN models. Similarly, satellite-based SST, ORA-based SSS data, geographical coordinates, and
 314 climatological TSL and OHC data were extracted by collocating with Kelvin-scaled in-situ OHC data for our ANN models to
 315 generate the OHC estimates. Evaluation of these two OHC estimates was done separately by means of the normalized metrics
 316 such as R, MBPE, and MAPE (Table 4).

317 **Table 4.** Statistical results observed during the validation of model-derived OHC estimates against in-situ OHC data.

Depth (m)	N	R		MBPE (%)		MAPE (%)	
		NRSC-ANN model	Proposed ANN model	NRSC-ANN model	Proposed ANN model	NRSC-ANN model	Proposed ANN model
50	15595	0.9223	0.9303	-0.0012	0.0227	1.4762	0.1104
100	14546	0.8575	0.8780	-0.3539	0.0303	2.5145	0.1732
150	14303	0.7678	0.8215	-0.6887	-0.0263	3.2401	0.2053
200	13513	0.7169	0.8152	-1.1048	0.0072	3.4667	0.1903
300	12833	0.7732	0.8690	-1.2656	0.0218	3.1671	0.1525
500	12410	0.8965	0.9346	-0.6996	-0.0052	2.3939	0.1073
700	11959	0.9447	0.9628	-0.6214	-0.0370	2.0035	0.0891

318

319

320 As expected, our ANN models produced relatively high accurate OHC estimates at all depth extents and hence yielded
321 higher correlation coefficients and lower errors as compared to the NRSC-ANN models. The accuracy of OHC estimates
322 produced by our ANN model also increased with depth in contrast to that of NRSC-ANN OHC estimates. Determination of
323 key input parameters based on a precise theoretical basis, accurate computation of in-situ OHC, and use of suitable ANN
324 architectures for each modeling depth enabled our ANN models to produce accurate OHC estimates.

325 It should be mentioned that SSHA is the combined outcome of temperature (thermohaline), salinity (halohaline), and
326 water mass changes in the oceanic water column. The direct use of satellite altimeter-derived SSHA without eliminating
327 halohaline and water mass change components results in weaker correlations with OHC. Moreover, the different time spans
328 were used in the computation of the mean sea level at AVISO (1993-2012) and monthly climatology data at WOA09 (1955-
329 2006). The combination of merged SSHA data from AVISO/CMEMS and climatological OHC data from WOA could lead to
330 discrepancies in OHC estimates. Hence, the prime criterion followed in determining the input parameters in the current study
331 is the theoretical relationship between the input and output parameters rather than the direct usage of all the relevant parameters.
332 The one-to-one relationship between OHC and TSL is employed in the OHC modeling. To arrive at TSL, the theoretical
333 dependency of TSL on temperature, salinity, and geographical coordinates is considered in TSL modeling work. However,
334 SSHA and climatological OHC data of the same base period are desirable and can be used in OHC (TSL) modeling if available
335 in the future.

336 Celsius scale can be used to compute in-situ OHC where the temperature is always on the positive side. The usage of
337 the Celsius scale when the temperatures are less than zero and greater than the seawater freezing point is not appropriate
338 because of the negative values. In addition, the conservative temperature is an accurate variable to calculate OHC compared
339 to the measured in-situ temperature or potential temperature (IOC et al., 2010; Pawlowicz, 2013). Thus, conservative
340 temperatures in the absolute scale (Kelvin scale) are used to compute in-situ OHC estimates in the current study. On the other
341 hand, employing instantaneous density rather than average density value is important to account for the dynamic variations in
342 seawater density.

343 The vertical distribution of conservative temperature follows a non-linear profile with a mixed layer at the top, a
344 thermocline at the middle, and a deep ocean layer at the bottom. This suggests that it is appropriate to customize the ANN
345 hyperparameters for each modeling depth. In this study, hyperparameter tuning was performed for each modeling depth and it
346 resulted in a better understanding of OHC patterns at various depth extents. Though a clear improvement was achieved with
347 the proposed OHC models, relatively lower correlations were observed for our ANN models in the depth range of 100-300 m
348 over the North Indian Ocean (refer to Table 4). It indicates that the ANN models less generalized the OHC patterns at the
349 intermediate depths over the North Indian Ocean and the corresponding underlying factors are discussed in the following
350 section. Nevertheless, the observed results demonstrated that the proposed ANN models are capable of improving the accuracy
351 and quality of OHC products through the ocean thermal expansion method.

352 **4.4. Potential sources of uncertainty in OHC estimates**

353 The relationship between the surficial parameters (SST and SSS) and depth-integrated parameters (TSL and OHC) is the prime
354 factor determining the efficiency of the proposed OHC models of various depth extents (Klemas and Yan, 2014). This
355 relationship is expected to account for a wide range of geophysical processes including ocean currents, vertical mixing
356 (upwelling/downwelling), stratification, fronts, gyres, eddies, and air-sea interface processes. In addition, different climate
357 modes and oscillations, solar radiation, sea ice, phytoplankton growth, freshwater inputs, and winds can also be considered in
358 this context. Monthly climatological CTD profiles obtained from WOA-18 were objectively analyzed to calculate the mean
359 SST and SSS fields over a period of 1955-2017. Hence, these climatological data along with real-time SST and SSS data
360 enabled the ANN models to better generalize the prevailing geophysical processes and subsequent patterns in TSL & OHC of
361 various depth extents. The same can be perceived from the improved accuracy levels observed during the validations carried
362 out on unseen data (refer to Sects. 4.1 and 4.2) and the comparison with NRSC-OHC products (Sect. 4.3).

363 It should be noted that the established relationship between the input parameters (surficial and climatological) and
364 output parameters (TSL & OHC patterns) may not hold great in the events of complex geophysical processes where the
365 physical oceanographic conditions differ significantly from the prevailing conditions. Moreover, the relative contributions of
366 these geophysical processes are subject to vary depending on the time and location of the water parcel in oceans. The slightly
367 lower accuracy of the proposed ANN models can be attributed to the influence of these complex geophysical processes. The
368 in-situ and satellite-based retrieval of all these atmospheric/surface/subsurface processes and their incorporation into the ANN
369 models is difficult because of the scarcity/sparsity of the required datasets in different spatial, temporal, and vertical scales.
370 The above factors constitute a potential source of uncertainty in OHC estimates and reduce the generalization ability of the
371 model. Hence, it is advisable to carry out vicarious calibration with the help of contemporary in-situ CTD profiles before
372 adopting the OHC estimates for further scientific analyses of specific interest in both regional and global scales. Further efforts
373 are needed to better understand, quantify, and eliminate the different sources of identified uncertainties caused by the complex
374 geophysical processes. More number of in-situ CTD profiles are required to be collected and analyzed in such oceanic regions
375 to better account for the associated complex patterns and processes.

376 **5. Spatiotemporal variability of OHC**

377 Here, we present the long-term variability of model-derived OHC and its comparison with the existing global OHC products
378 for the period 1993-2020. The time period (1993-2020) was chosen based on the availability of satellite-based input data to
379 generate the model-derived OHC estimates and the existing OHC products considered. Thus, model-derived OHC estimates
380 were generated from 1993 to 2020 at a spatial resolution of 0.25° and computed annual time series of model-derived OHC
381 anomalies (OHCA) with reference to the 1993-2020 long-term mean. It is worth mentioning that the model-derived OHCA
382 estimates presented in this section represent heat changes in both shallower and deep oceanic basins of bathymetry levels ≥ 20
383 m. The bathymetry values of each pixel were rounded off to the nearest and lowest modeling depth (d) with the help of

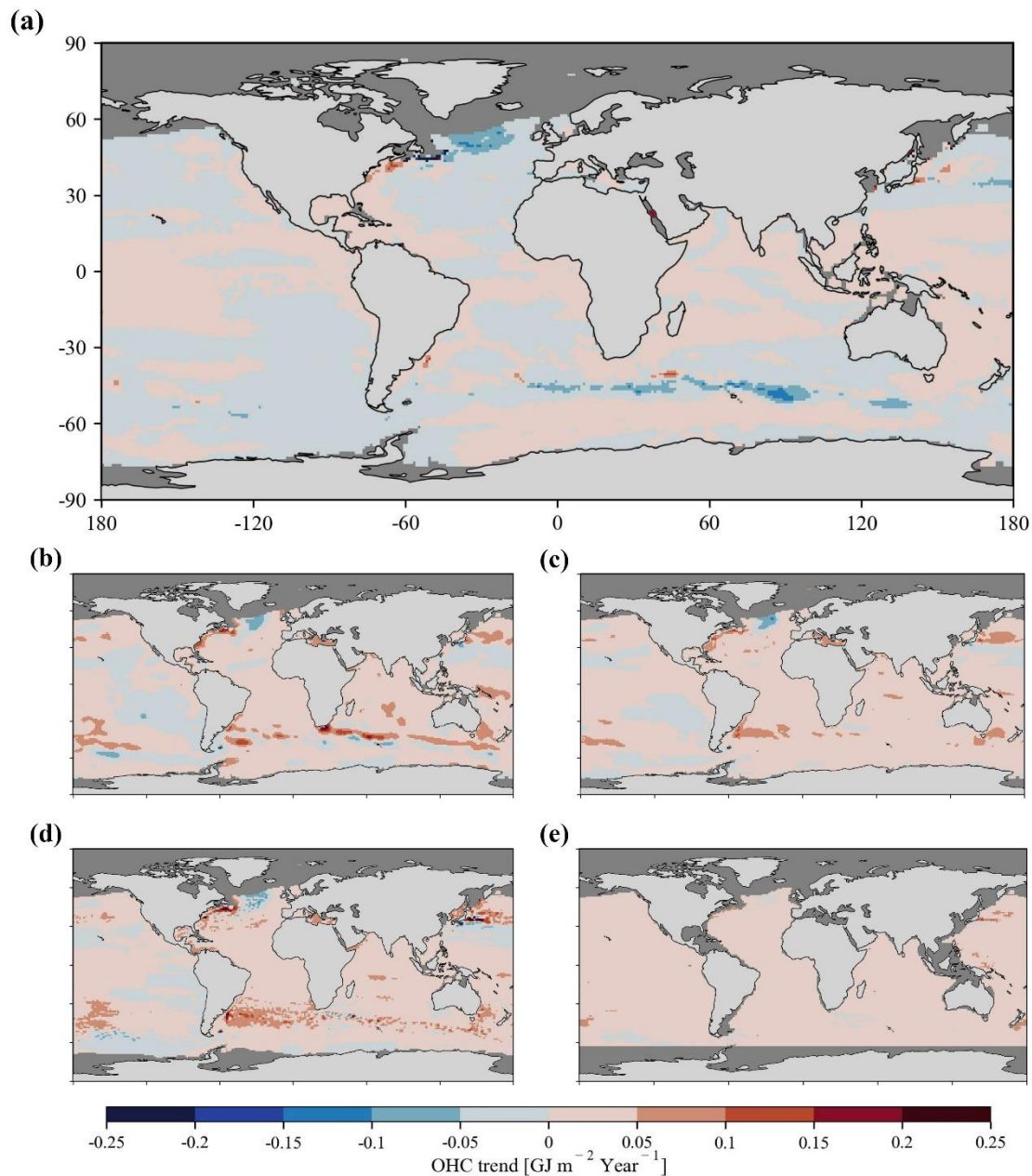
384 GEBCO-2020 bathymetry data, and the corresponding OHCA_d values were considered for that pixel (GEBCO Compilation
385 Group, 2020).

386 On the other hand, OHCA time series annual maps obtained from various global OHC products such as the National
387 Centers for Environmental Information (NCEI), Institute of Atmospheric Physics (IAP), Pacific Marine Environmental
388 Laboratory (PMEL), and OPEN-LSTM have been employed for comparison. NCEI employs the Objective analysis method
389 on in-situ CTD profile data of World Ocean Database-2009 and estimates annual OHCA at a spatial resolution of 1° with
390 reference to the 1955-2006 long-term mean (Levitus et al., 2012). Similarly, IAP employs the ensemble optimal interpolation
391 with a dynamic ensemble approach on in-situ CTD profile data of World Ocean Database-2013 and distributes monthly OHC
392 estimates at a spatial resolution of 1° (Cheng et al., 2017). Annual OHC means were computed from IAP monthly OHC data,
393 and annual OHCA estimates were generated with reference to the 1993-2020 long-term mean. Recently, PMEL has developed
394 a random forest regression model to predict OHCA of 0-40 m, 40-90 m, 90-190 m, 190-290 m, 290-450 m, 450-700 m, 700-
395 950 m, 950-1450 m, etc with reference to the 1993-2022 long-term mean. This PMEL random forest regression model employs
396 satellite-based SST, SSHA, latitude, longitude, and time data to predict weekly OHCA estimates at a spatial resolution of 0.25°
397 (Lyman and Johnson, 2023). In the current study, PMEL layer-wise OHCA estimates from surface to 700 m have been summed
398 up at each pixel to arrive at weekly OHCA spatial maps and subsequently computed corresponding annual OHCA estimates.
399 Similarly, Su et al., (2021) have developed a long short-term memory neural network method to produce monthly OHC
400 estimates (OPEN-LSTM) at a spatial resolution of 1°. OPEN-LSTM employs satellite-based SSHA, SST, zonal and meridional
401 components of sea surface wind, latitude, longitude, and day of the year to predict monthly OHC. Annual OHC means were
402 computed from OPEN-LSTM monthly OHC data, and annual OHCA estimates were generated with reference to the 1993-
403 2020 long-term mean.

404 Model-derived annual OHCA estimates were regridded to 1° spatial resolution to maintain uniform spatial reference
405 among all the OHC products considered. As the proposed models are built for open oceanic regions, the regions covered by
406 sea ice are masked in both the north and south poles by verifying the corresponding sea ice concentration data obtained from
407 the National Snow and Ice Data Center (Meier et al., 2021). Subsequently, long-term variability maps (Fig. 8) and time series
408 plots (Fig. 9) were produced to compare model-derived OHC estimates with the existing global OHC products. Further, the
409 information on percentage variance explained (PVE) by the observed long-term trend values is provided to realise the short-
410 term trends or periodic signals in OHC variability (Fig. A4). Higher PVE values indicate the persistent increase or decrease in
411 OHC throughout the study period, and vice versa.

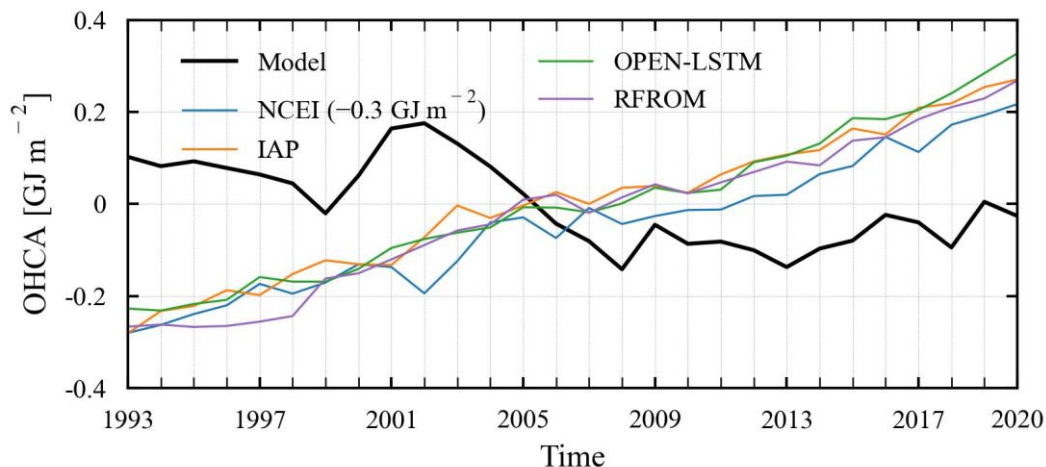
412 Lower magnitudes of long-term warming/cooling trends ($\pm 0.05 \text{ GJ m}^{-2} \text{ Year}^{-1}$) are observed throughout the global
413 ocean (Fig. 8a). The corresponding PVE values are observed to be very low ($\leq 30\%$) which infer the intermittent trends in
414 majority of the global ocean rather than persistent warming/cooling (Fig. A4a). The same can be observed from the non-linear
415 distribution of OHCA time series indicating short-term periods of alternate warming and cooling during the study period (Fig.
416 9). However, the oceanic regions linked with Kuroshio current, Gulf stream, Antarctic circumpolar current, North Atlantic

417 cold blob, southeastern Pacific are experiencing relatively higher magnitudes of persistent warming/cooling (± 0.1 to 0.15 GJ
418 $\text{m}^{-2} \text{Year}^{-1}$, PVE 50-90%).



419
420 **Figure 8.** Spatial maps showing the long-term trends of OHC obtained from (a) the current model, (b) NCEI, (c) IAP, (d)
421 PMEL, and (e) OPEN-LSTM products. Note that the oceanic regions shallower than 20 m depth and/or covered with sea ice
422 are masked with a dark gray color.
423

424 The spatial patterns of OHC trends observed from NCEI (Fig. 8b), IAP (Fig. 8c), and PMEL (Fig. 8d) products are
 425 almost similar and relatively more warming regions compared to the model-derived OHC estimates (Fig. 8a). NCEI, IAP, and
 426 PMEL products indicating persistent warming conditions over the vast oceanic regions of the Pacific, Atlantic, and Indian
 427 Oceans with higher PVE values (Figs. A4b-A4d). The same can be observed from the persistent long-term warming throughout
 428 the study period (Fig. 9). On the other hand, OPEN-LSTM OHC estimates indicate lower warming patterns all over the globe
 429 except the North Atlantic cold blob and some parts of the Antarctic circumpolar current (Fig. 8e) with higher PVE values over
 430 vast oceanic regions of Pacific, Atlantic, and Indian Oceans (Fig. A4e). As a result, OPEN-LSTM also showed persistent long-
 431 term warming throughout the study period (Fig. 9).



432
 433 **Figure 9.** Time series distribution of global mean OHCA obtained from the current model and the existing OHC products
 434 observed over the period 1993-2020. Note that the NCEI time series has been shifted by subtracting 0.3 GJ m^{-2} to better
 435 compare with the remaining OHC time series plots.

436 The observed time series plots have indicated contrasting trends between the current OHC model and the existing
 437 products. The time series plot of model-derived OHCA has indicated alternate periods of short-term cooling and warming
 438 during the study period. Global open oceans have witnessed a cooling trend of $-0.017 \text{ GJ m}^{-2} \text{ Year}^{-1}$ (PVE 76.99%) during
 439 1993-1999, a warming trend of $+0.069 \text{ GJ m}^{-2} \text{ Year}^{-1}$ (PVE 92.73%) during 2000-2002, a cooling trend of $-0.054 \text{ GJ m}^{-2} \text{ Year}^{-1}$
 440 $^{-1}$ (PVE 99.71%) during 2003-2008, and a warming trend of $+0.007 \text{ GJ m}^{-2} \text{ Year}^{-1}$ (PVE 36.50%) during 2009-2020. The
 441 observed results indicate the efficiency of the current model by capturing the ocean cooling during 2003-2006 (Loehle, 2009;
 442 Lyman et al., 2006) and the global warming hiatus during 1998-2013 (Trenberth, 2015). Whereas the observed time series
 443 plots of NCEI, IAP, PMEL, and OPEN-LSTM products indicated persistent warming trends of $+0.017 \text{ GJ m}^{-2} \text{ Year}^{-1}$ (PVE
 444 95.75%), $+0.019 \text{ GJ m}^{-2} \text{ Year}^{-1}$ (PVE 97.94%), $+0.0198 \text{ GJ m}^{-2} \text{ Year}^{-1}$ (PVE 97.19%), and $+0.0195 \text{ GJ m}^{-2} \text{ Year}^{-1}$ (PVE
 445 97.48%), respectively. However, full-depth pan-global OHCA estimates by including OHC estimates over ice-covered oceanic
 446 regions are required to substantiate these global ocean cooling and global warming hiatus signatures, and to realize the role of
 447 excess heat added by anthropogenic climate change.

448 6. Conclusion

449 Accurate reconstruction of OHC and analysis of its regional patterns and long-term global records are critical for estimating
450 the Earth's energy imbalance and understanding the evolution of climate change. Owing to the lack of instrumentation to cover
451 geographic and depth ranges, OHC estimates from the in-situ measured temperatures are temporally limited and insufficiently
452 widespread to capture its spatiotemporal changes and structures. OHC estimates from either different mapping methods or
453 Ocean reanalyses (ORAs) have yielded large uncertainties in past studies. Thus, improving OHC estimates through a novel
454 satellite-based method is the major step forward in overcoming sparse observations and reducing the uncertainty in OHC
455 trends. In this study, we proposed an artificial network model to estimate OHC changes in global oceans. The proposed ANN
456 model incorporates the ocean thermal expansion method as a promising tool to estimate OHC changes from satellite data.
457 Accurate implementation of the ocean thermal expansion method was challenging due to the inability of the present-day
458 satellite systems to directly measure the ocean thermal expansion/contraction component. In this study, we proposed a satellite-
459 based novel approach to better implement the ocean thermal expansion method by establishing a relationship between the
460 surficial parameters such as SST & SSS and subsurface T-S profiles. This model predicts the depth-integrated TSL component
461 by making use of SST & SSS data and then utilizes the predicted TSL to estimate OHC changes. For this application, we
462 developed ANN models for TSL and OHC of various depth extents such as 20 m, 30 m, 40 m, 50 m, 100 m, 150 m, 200 m,
463 250 m, 300 m, 350 m, 400 m, 450 m, 500 m, 550 m, 600 m, 650 m, and 700 m. The performance of these TSL & OHC models
464 was assessed by carrying out in-situ-based and satellite-based validations by using the unseen in-situ CTD profiles from the
465 Argo program. Observed high correlations and low errors indicated that the proposed ANN models performed exceptionally
466 good on unseen data of all modeling depths without any overfitting and can be used in conjunction with the sea ice
467 thermodynamics-based OHC models of the ice-covered oceans (Vijay and Shanmugam, 2022) to better study the pan-global
468 OHC changes by covering both open and ice-covered oceanic regions of varying bathymetry levels (≥ 20 m).

469 The model development and validation databases were prepared by using in-situ CTD profiles obtained from the Argo
470 program and collocated with the corresponding satellite-based daily data of SST (AVHRR v2.1) and SSS (ORAS5). The
471 multilayer perceptron regressor algorithm of deep neural networks was used and its architecture was optimized by evaluating
472 different combinations of hyperparameters for each modeling depth using the particle swarm optimization technique. Precise
473 consideration of theoretical aspects in the selection of input parameters, accurate computation of in-situ OHC, and customized
474 ANN architectures enabled the proposed models to establish the accurate relationships between the surficial parameters and
475 depth-integrated OHC (TSL) of various depths extents. The overall performance of the proposed models on satellite data was
476 good, suggesting that these models can be used for a variety of applications subjected to the accuracy requirements and can
477 produce accurate satellite-based OHC (TSL) estimates at various depth extents than previously possible. However, the
478 influence of complex geophysical processes on the generalization ability of ANN models is discussed, and realized that the
479 proposed models relatively less generalized the data in the events of complex geophysical processes. Further research should
480 focus on implementation of these models over the oceanic regions with complex geophysical processes. More number of in-

481 situ CTD profiles need to be collected and analyzed in such oceanic regions to better account the associated complex patterns.
482 However, the scope of the current research includes minimizing the observed marginal gap by exploring new
483 methods/parametrizations in satellite-based OHC modeling approaches.

484 **CRedit authorship contribution statement**

485 **Vijay Prakash Kondeti:** Conceptualization, Data curation, Formal analysis, Funding acquisition, Investigation, Methodology,
486 Software, Validation, Visualization, and Writing - original draft. **Palanisamy Shanmugam:** Conceptualization, Formal
487 analysis, Funding acquisition, Investigation, Methodology, Project administration, Resources, Supervision, and Writing -
488 review & editing.

489 **Code and Data availability**

490 Data will be made available on request.

491 **Declaration of competing interest**

492 The authors declare no known competing financial or personal interests in this paper.

493 **Acknowledgement**

494 This research work was supported by The Prime Minister's Research Fellows (PMRF) Scheme and in part by the National
495 Geospatial Programme (NGP) of Department of Science and Technology of Government of India (Grant No:
496 OEC1819150DSTXPSHA). The authors are thankful to the Argo program for providing in-situ CTD profiles. They are grateful
497 to NOAA for WOD-18, WOA-18, and SST data; CMEMS for SSS data; NCEI, IAP, PMEL, and Science Data Bank for OHC
498 estimates; NSIDC for sea ice concentration data; and GEBCO for bathymetry data. The authors are thankful to the two
499 anonymous researchers for their constructive comments and recommendations.

500

501 **References**

502 Abraham, J. P., Baringer, M., Bindoff, N. L., Boyer, T., Cheng, L. J., Church, J. A., Conroy, J. L., Domingues, C. M., Fasullo,
503 J. T., Gilson, J., Goni, G., Good, S. A., Gorman, J. M., Gouretski, V., Ishii, M., Johnson, G. C., Kizu, S., Lyman, J. M.,
504 Macdonald, A. M., Minkowycz, W. J., Moffitt, S. E., Palmer, M. D., Piola, A. R., Reseghetti, F., Schuckmann, K., Trenberth,
505 K. E., Velicogna, I., and Willis, J. K.: A review of global ocean temperature observations: Implications for ocean heat content
506 estimates and climate change, *Rev. Geophys.*, 51, 450–483, <https://doi.org/10.1002/rog.20022>, 2013.
507 Ali, M. M., Jagadeesh, P. S. V., Lin, I. I., and Hsu, J. Y.: A neural network approach to estimate tropical cyclone heat potential
508 in the Indian Ocean, *IEEE Geosci. Remote Sens. Lett.*, 9, 1114–1117, <https://doi.org/10.1109/LGRS.2012.2190491>, 2012.

509 Balmaseda, M. A., Hernandez, F., Storto, A., Palmer, M. D., Alves, O., Shi, L., Smith, G. C., Toyoda, T., Valdivieso, M.,
510 Barnier, B., Behringer, D., Boyer, T., Chang, Y. S., Chepurin, G. A., Ferry, N., Forget, G., Fujii, Y., Good, S., Guinehut, S.,
511 Haines, K., Ishikawa, Y., Keeley, S., Köhl, A., Lee, T., Martin, M. J., Masina, S., Masuda, S., Meyssignac, B., Mogensen, K.,
512 Parent, L., Peterson, K. A., Tang, Y. M., Yin, Y., Vernieres, G., Wang, X., Waters, J., Wedd, R., Wang, O., Xue, Y., Chevallier,
513 M., Lemieux, J. F., Dupont, F., Kuragano, T., Kamachi, M., Awaji, T., Caltabiano, A., Wilmer-Becker, K., and Gaillard, F.:
514 The ocean reanalyses intercomparison project (ORA-IP), *J. Oper. Oceanogr.*, 8, s80–s97,
515 <https://doi.org/10.1080/1755876X.2015.1022329>, 2015.

516 Baxter, J. M.: Explaining Ocean Warming: Causes, scale, effects and consequences, edited by: Laffoley, D. and Baxter, J. M.,
517 IUCN, International Union for Conservation of Nature, <https://doi.org/10.2305/IUCN.CH.2016.08.en>, 2016.

518 Beech, N., Rackow, T., Semmler, T., Danilov, S., Wang, Q., and Jung, T.: Long-term evolution of ocean eddy activity in a
519 warming world, *Nat. Clim. Chang.*, 12, 910–917, <https://doi.org/10.1038/s41558-022-01478-3>, 2022.

520 Boyer, T. P., Baranova, O. K., Coleman, C., Garcia, H. E., Grodsky, A., Locarnini, R. A., Mishonov, A. V., Paver, C. R.,
521 Reagan, J. R., Seidov, D., Smolyar, I. V., Weathers, K. W., and Zweng, M. M.: NOAA Atlas NESDIS 87. World Ocean
522 Database 2018, 1–207, 2018.

523 Chacko, N., Dutta, D., Ali, M. M., Sharma, J. R., and Dadhwa, V. K.: Near-real-time availability of ocean heat content over
524 the north indian ocean, *IEEE Geosci. Remote Sens. Lett.*, 12, 1033–1036, <https://doi.org/10.1109/LGRS.2014.2375196>, 2015.

525 Chambers, D. P., Tapley, B. D., and Stewart, R. H.: Long-period ocean heat storage rates and basin-scale heat fluxes from
526 TOPEX, *J. Geophys. Res. Ocean.*, 102, 10525–10533, <https://doi.org/10.1029/96JC03644>, 1997.

527 Cheng, L., Zhu, J., and Srivier, R. L.: Global representation of tropical cyclone-induced ocean thermal changes using Argo data
528 – Part 2: Estimating air – sea heat fluxes and ocean heat content changes, *Ocean Sci. Discuss.*, 11, 2907–2937,
529 <https://doi.org/10.5194/osd-11-2907-2014>, 2014.

530 Cheng, L., Trenberth, K. E., Fasullo, J., Boyer, T., Abraham, J., and Zhu, J.: Improved estimates of ocean heat content from
531 1960 to 2015, *Sci. Adv.*, 3, 1–10, <https://doi.org/10.1126/sciadv.1601545>, 2017.

532 Cheng, L., Foster, G., Hausfather, Z., Trenberth, K. E., and Abraham, J.: Improved Quantification of the Rate of Ocean
533 Warming, *J. Clim.*, 35, 4827–4840, <https://doi.org/10.1175/jcli-d-21-0895.1>, 2022.

534 Huang, B., Liu, C., Banzon, V., Freeman, E., Graham, G., Hankins, B., Smith, T., and Zhang, H. M.: Improvements of the
535 Daily Optimum Interpolation Sea Surface Temperature (DOISST) Version 2.1, *J. Clim.*, 34, 2923–2939,
536 <https://doi.org/10.1175/JCLI-D-20-0166.1>, 2021.

537 IOC, SCOR, and IAPSO: The international thermodynamic equation of seawater-2010: Calculation and use of thermodynamic
538 properties Intergovernmental Oceanographic Commission, 2010.

539 IPCC: Climate Change 2014: Synthesis Report. Contribution of Working Groups I, II and III to the Fifth Assessment Report
540 of the Intergovernmental Panel on Climate Change, *J. Cryst. Growth*, 2014.

541 IPCC: Changing Ocean, Marine Ecosystems, and Dependent Communities, 447–588 pp.,
542 <https://doi.org/10.1017/9781009157964.013>, 2022.

543 Irrgang, C., Saynisch, J., and Thomas, M.: Estimating global ocean heat content from tidal magnetic satellite observations,
544 *Sci. Rep.*, 9, 1–8, <https://doi.org/10.1038/s41598-019-44397-8>, 2019.

545 Jagadeesh, P. S. V. and Ali, M. M.: Estimation of upper ocean heat content from remote sensing observations in the Arabian
546 Sea, *Remote Sens. Model. Atmos. Ocean. Interact.*, 6404, 64041C, <https://doi.org/10.1117/12.699319>, 2006.

547 Jagadeesh, P. S. V., Suresh Kumar, M., and Ali, M. M.: Estimation of Heat Content and Mean Temperature of Different Ocean
548 Layers, *IEEE J. Sel. Top. Appl. Earth Obs. Remote Sens.*, 8, 1251–1255, <https://doi.org/10.1109/JSTARS.2015.2403877>,
549 2015.

550 Kennedy, J., & Eberhart, R.: Particle Swarm Optimization, in: In Proceedings of ICNN'95-international conference on neural
551 networks, IEEE, 1942–1948, https://doi.org/10.1007/978-3-319-46173-1_2, 1995.

552 Klemas, V. and Yan, X. H.: Subsurface and deeper ocean remote sensing from satellites: An overview and new results, *Prog.*
553 *Oceanogr.*, 122, 1–9, <https://doi.org/10.1016/j.pocean.2013.11.010>, 2014.

554 L'Ecuyer, T. S., Beadoing, H. K., Rodell, M., Olson, W., Lin, B., Kato, S., Clayson, C. A., Wood, E., Sheffield, J., Adler, R.,
555 Huffman, G., Bosilovich, M., Gu, G., Robertson, F., Houser, P. R., Chambers, D., Famiglietti, J. S., Fetzer, E., Liu, W. T.,
556 Gao, X., Schlosser, C. A., Clark, E., Lettenmaier, D. P., and Hilburn, K.: The observed state of the energy budget in the early
557 twenty-first century, *J. Clim.*, 28, 8319–8346, <https://doi.org/10.1175/JCLI-D-14-00556.1>, 2015.

558 Levitus, S., Antonov, J. I., Boyer, T. P., Locarnini, R. A., Garcia, H. E., and Mishonov, A. V.: Global ocean heat content 1955-
559 2008 in light of recently revealed instrumentation problems, *Geophys. Res. Lett.*, 36, 1–5,
560 <https://doi.org/10.1029/2008GL037155>, 2009.

561 Levitus, S., Antonov, J. I., Boyer, T. P., Baranova, O. K., Garcia, H. E., Locarnini, R. A., Mishonov, A. V, Reagan, J. R.,
562 Seidov, D., Yarosh, E. S., and Zweng, M. M.: World ocean heat content and thermosteric sea level change (0–2000 m), 1955–
563 2010, *Geophys. Res. Lett.*, 39, 1–5, <https://doi.org/10.1029/2012GL051106>, 2012.

564 Liang, X., Wunsch, C., Heimbach, P., and Forget, G.: Vertical redistribution of oceanic heat content, *J. Clim.*, 28, 3821–3833,
565 <https://doi.org/10.1175/JCLI-D-14-00550.1>, 2015.

566 Loehle, C.: Cooling of the global ocean since 2003, *Energy Environ.*, 20, 101–104,
567 <https://doi.org/10.1260/095830509787689141>, 2009.

568 Lyman, J. M. and Johnson, G. C.: Global High-Resolution Random Forest Regression Maps of Ocean Heat Content Anomalies
569 Using In Situ and Satellite Data, *J. Atmos. Ocean. Technol.*, 40, 575–586, <https://doi.org/10.1175/JTECH-D-22-0058.1>, 2023.

570 Lyman, J. M., Willis, J. K., and Johnson, G. C.: Recent cooling of the upper ocean, *Geophys. Res. Lett.*, 33, 1–5,
571 <https://doi.org/10.1029/2006GL027033>, 2006.

572 Marti, F., Blazquez, A., Meyssignac, B., Ablain, M., Barnoud, A., Fraudeau, R., Jugier, R., Chenal, J., Larnicol, G., Pfeffer,
573 J., Restano, M., and Benveniste, J.: Monitoring the ocean heat content change and the Earth energy imbalance from space
574 altimetry and space gravimetry, *Earth Syst. Sci. Data*, 14, 229–249, <https://doi.org/10.5194/essd-14-229-2022>, 2022.

575 Meyssignac, B., Boyer, T., Zhao, Z., Hakuba, M. Z., Landerer, F. W., Stammer, D., Köhl, A., Kato, S., L'Ecuyer, T., Ablain,
576 M., Abraham, J. P., Blazquez, A., Cazenave, A., Church, J. A., Cowley, R., Cheng, L., Domingues, C., Giglio, D., Gouretski,

577 V., Ishii, M., Johnson, G. C., Killick, R. E., Legler, D., Llovel, W., Lyman, J., Palmer, M. D., Piotrowicz, S., Purkey, S.,
578 Roemmich, D., Roca, R., Savita, A., Schuckmann, K. von, Speich, S., Stephens, G., Wang, G. G., Wijffels, S. E., and
579 Zilberman, N.: Measuring global ocean heat content to estimate the earth energy imbalance, *Front. Mar. Sci.*, 6, 1–31,
580 <https://doi.org/10.3389/fmars.2019.00432>, 2019.

581 Momin, I. M., Sharma, R., and Basu, S.: Satellite-derived heat content in the tropical Indian Ocean, *Remote Sens. Lett.*, 2,
582 269–277, <https://doi.org/10.1080/01431161.2010.519001>, 2011.

583 Ni, Q., Zhai, X., LaCasce, J. H., Chen, D., and Marshall, D. P.: Full-Depth Eddy Kinetic Energy in the Global Ocean Estimated
584 From Altimeter and Argo Observations, *Geophys. Res. Lett.*, 50, <https://doi.org/10.1029/2023GL103114>, 2023.

585 Palmer, M. D., Roberts, C. D., Balmaseda, M., Chang, Y. S., Chepurin, G., Ferry, N., Fujii, Y., Good, S. A., Guinehut, S.,
586 Haines, K., Hernandez, F., Köhl, A., Lee, T., Martin, M. J., Masina, S., Masuda, S., Peterson, K. A., Storto, A., Toyoda, T.,
587 Valdivieso, M., Vernieres, G., Wang, O., and Xue, Y.: Ocean heat content variability and change in an ensemble of ocean
588 reanalyses, *Clim. Dyn.*, 49, 909–930, <https://doi.org/10.1007/s00382-015-2801-0>, 2017.

589 Pedregosa, F., Varoquaux, G., Gramfort, A., Michel, V., Thirion, B., Grisel, O., Blondel, M., Prettenhofer, P., Weiss, R.,
590 Dubourg, V., and Vanderplas, J.: Scikit-learn: Machine learning in Python, *J. Mach. Learn. Res.*, 12, 2825–2830, 2011.

591 Polito, P. S., Sato, O. T., and Liu, W. T.: Characterization and validation of the heat storage variability from TOPEX/Poseidon
592 at four oceanographic sites, *J. Geophys. Res. Ocean.*, 105, 16911–16921, <https://doi.org/10.1029/1999JC000048>, 2000.

593 Resplandy, L., Keeling, R. F., Eddebbar, Y., Brooks, M. K., Wang, R., Bopp, L., Long, M. C., Dunne, J. P., Koeve, W., and
594 Oschlies, A.: Quantification of ocean heat uptake from changes in atmospheric O₂ and CO₂ composition, *Nature*, 563, 105–
595 108, <https://doi.org/10.1038/s41586-018-0651-8>, 2018.

596 Riser, S. C., Freeland, H. J., Roemmich, D., Wijffels, S., Troisi, A., Belbéoch, M., Gilbert, D., Xu, J., Pouliquen, S., Thresher,
597 A., Le Traon, P. Y., Maze, G., Klein, B., Ravichandran, M., Grant, F., Poulain, P. M., Suga, T., Lim, B., Sterl, A., Sutton, P.,
598 Mork, K. A., Vélez-Belchí, P. J., Ansorge, I., King, B., Turton, J., Baringer, M., and Jayne, S. R.: Fifteen years of ocean
599 observations with the global Argo array, *Nat. Clim. Chang.*, 6, 145–153, <https://doi.org/10.1038/nclimate2872>, 2016.

600 Roemmich, D., Church, J., Gilson, J., Monselesan, D., Sutton, P., and Wijffels, S.: Unabated planetary warming and its ocean
601 structure since 2006, *Nat. Clim. Chang.*, 5, 240–245, <https://doi.org/10.1038/nclimate2513>, 2015.

602 Sato, O. T., Polito, P. S., and Liu, W. T.: Importance of salinity measurements in the heat storage estimation from
603 TOPEX/POSEIDON, *Geophys. Res. Lett.*, 27, 549–551, <https://doi.org/10.1029/1999GL011003>, 2000.

604 Von Schuckmann, K., Palmer, M. D., Trenberth, K. E., Cazenave, A., Chambers, D., Champollion, N., Hansen, J., Josey, S.
605 A., Loeb, N., Mathieu, P. P., Meyssignac, B., and Wild, M.: An imperative to monitor Earth’s energy imbalance, *Nat. Clim.*
606 *Chang.*, 6, 138–144, <https://doi.org/10.1038/nclimate2876>, 2016.

607 Shi, Y., & Eberhart, R.: A Modified Particle Swarm Optimizer Algorithm, in: *IEEE international conference on evolutionary*
608 *computation proceedings*, 69–73, <https://doi.org/10.1109/ICEMI.2007.4350772>, 1998.

609 Su, H., Zhang, H., Geng, X., Qin, T., Lu, W., and Yan, X. H.: OPEN: A new estimation of global ocean heat content for upper
610 2000 meters from remote sensing data, *Remote Sens.*, 12, <https://doi.org/10.3390/rs12142294>, 2020.

611 Su, H., Qin, T., Wang, A., and Lu, W.: Reconstructing ocean heat content for revisiting global ocean warming from remote
612 sensing perspectives, *Remote Sens.*, 13, <https://doi.org/10.3390/rs13193799>, 2021.

613 Trenberth, K. E.: Has there been a hiatus?, *Science* (80-.), 349, 691–692, <https://doi.org/10.1126/science.aac9225>, 2015.

614 Trenberth, K. E., Fasullo, J. T., von Schuckmann, K., and Cheng, L.: Insights into Earth’s energy imbalance from multiple
615 sources, *J. Clim.*, 29, 7495–7505, <https://doi.org/10.1175/JCLI-D-16-0339.1>, 2016.

616 Trossman, D. S. and Tyler, R. H.: Predictability of Ocean Heat Content From Electrical Conductance, *J. Geophys. Res. Ocean.*,
617 124, 667–679, <https://doi.org/10.1029/2018JC014740>, 2019.

618 Vijay, P. K. and Shanmugam, P.: Artificial Neural Network Model for Estimating Ocean Heat Content in the Sea Ice-Covered
619 Arctic Regions Using Satellite Data, *IEEE Access*, 10, 109544–109557, <https://doi.org/10.1109/ACCESS.2022.3213942>,
620 2022.

621 White, W. B. and Tai, C.: Inferring interannual changes in global upper ocean heat storage from TOPEX altimetry, *J. Geophys.*
622 *Res. Ocean.*, 100, 24943–24954, <https://doi.org/10.1029/95JC02332>, 1995.

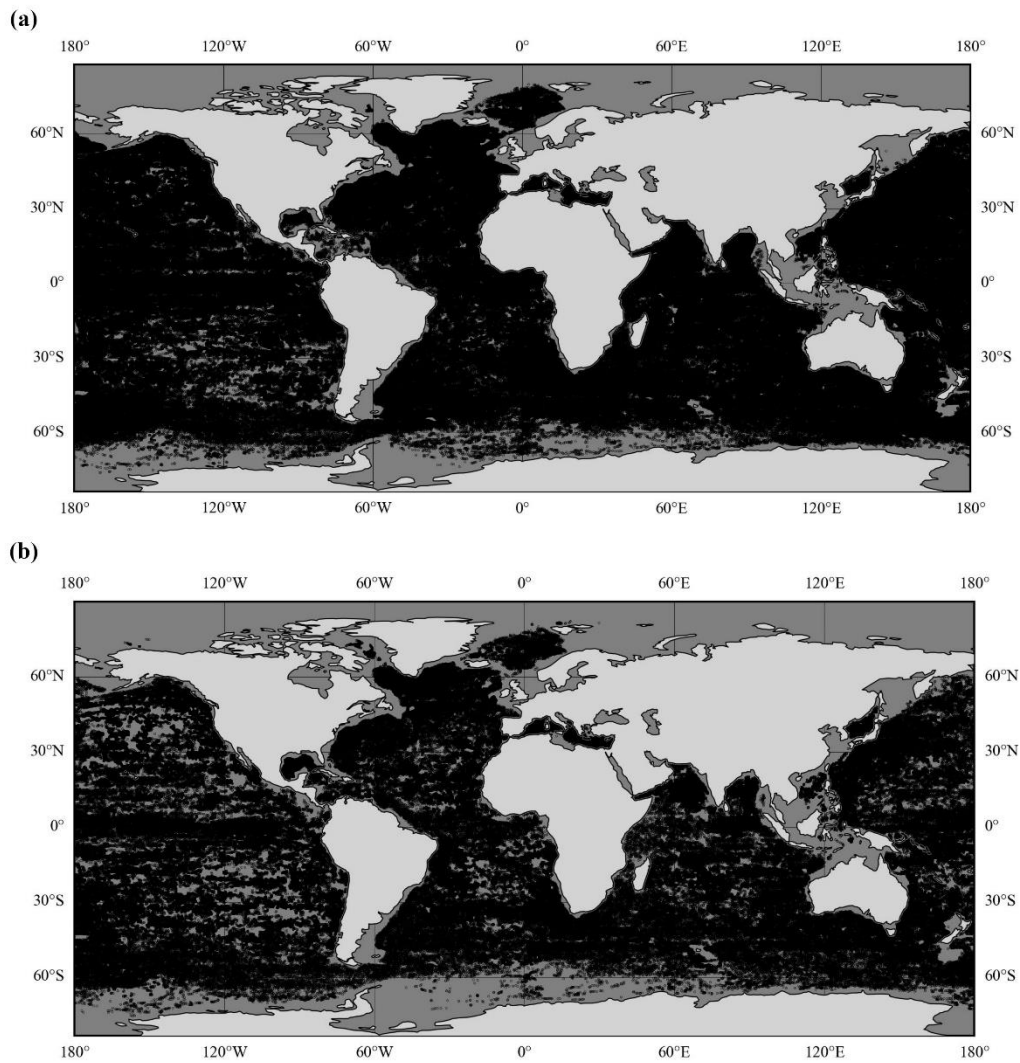
623 Wild, M., Folini, D., Hakuba, M. Z., Schär, C., Seneviratne, S. I., Kato, S., Rutan, D., Ammann, C., Wood, E. F., and König-
624 Langlo, G.: The energy balance over land and oceans: an assessment based on direct observations and CMIP5 climate models,
625 *Clim. Dyn.*, 44, 3393–3429, <https://doi.org/10.1007/s00382-014-2430-z>, 2015.

626 Zhao, Z.: Internal tide oceanic tomography, *Geophys. Res. Lett.*, 43, 9157–9164, <https://doi.org/10.1002/2016GL070567>,
627 2016.

628 Zhao, Z.: Propagation of the Semidiurnal Internal Tide: Phase Velocity Versus Group Velocity, *Geophys. Res. Lett.*, 44,
629 11,942-11,950, <https://doi.org/10.1002/2017GL076008>, 2017.

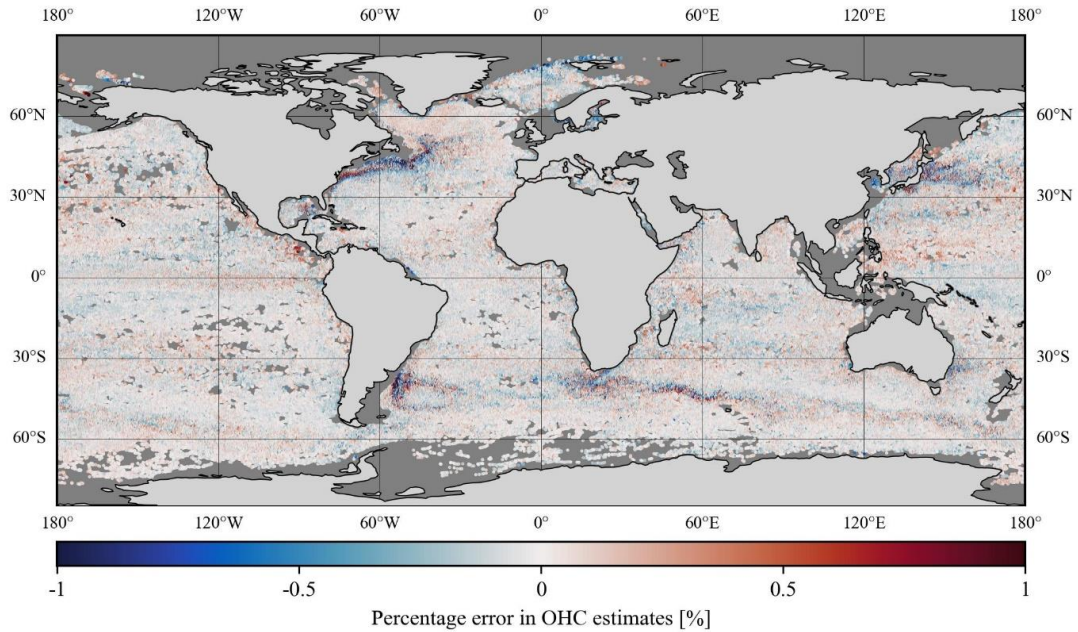
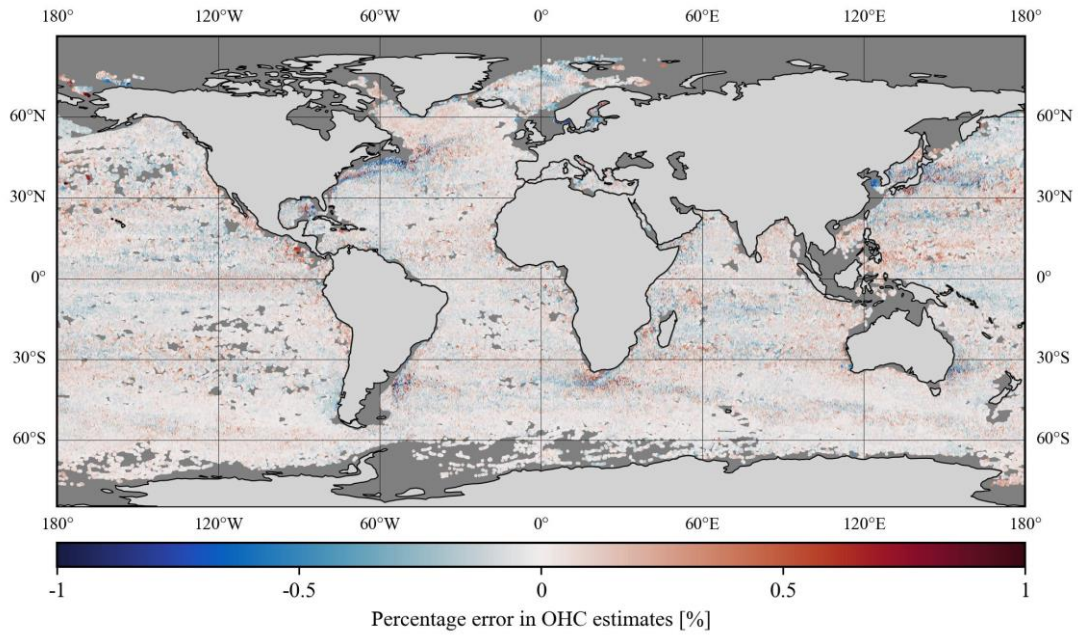
630 Zuo, H., Balmaseda, M. A., and Mogensen, K.: The new eddy-permitting ORAP5 ocean reanalysis: description, evaluation
631 and uncertainties in climate signals, *Clim. Dyn.*, 49, 791–811, <https://doi.org/10.1007/s00382-015-2675-1>, 2017.

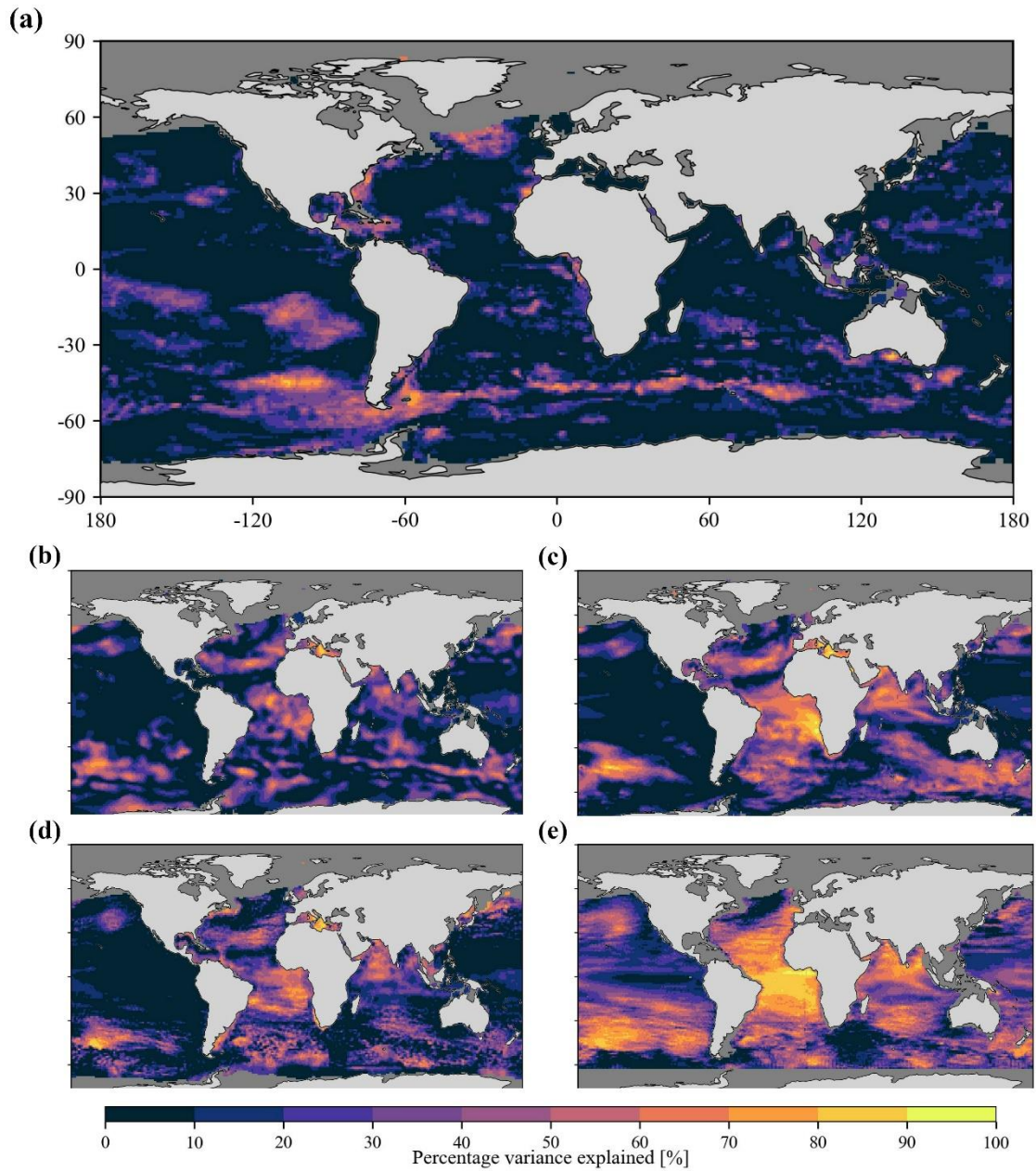
632
633
634
635
636
637
638
639
640
641
642
643
644



646
647 **Figure A1.** The spatial distribution of in-situ data points used for (a) model development (N=633004 Argo CTD profiles) and
648 (b) validation (N=388469 unseen Argo CTD profiles) in the case of TSL₇₀₀ and OHC₇₀₀.

649
650
651
652





661

662 **Figure A4.** Spatial maps showing the percentage variance explained by the OHC trends obtained from (a) the current model,
 663 (b) NCEI, (c) IAP, (d) PMEL, and (e) OPEN-LSTM products. Note that the oceanic regions shallower than 20 m depth and/or
 664 covered with sea ice are masked with a dark gray color.

665

666